Psychomotor Impairments and Therapeutic Implications Revealed by a Mutation Associated with Infantile Parkinsonism-Dystonia

Jenny I. Aguilar[1,2], Mary Hongying Cheng[3], Josep Font[4], Alexandra C. Schwartz[5], Kaitlyn Ledwitch[6,7], Amanda Duran[6,7], Samuel J. Mabry[2], Andrea N. Belovich[8], Yanqi Zhu[2], Angela M. Carter[2], Lei Shi[9], Manju A. Kurian[10], Cristina Fenollar-Ferrer[11], Jens Meiler[6,7,12], Renae M. Ryan[4], Hassane S. Mchaourab[5], Ivet Bahar[3], #Heinrich J. G. Matthies[2], #Aurelio Galli[2]

[1] Department of Pharmacology, Vanderbilt University, Nashville, TN, USA

[2] Department of Surgery, University of Alabama at Birmingham, Birmingham, AL, USA

[3] Department of Computational and Systems Biology, School of Medicine, University of Pittsburgh, Pittsburgh, PA, USA

[4] School of Medical Sciences, Faculty of Medicine and Health, University of Sydney, Sydney, NSW, Australia

[5] Department of Molecular Physiology & Biophysics, Vanderbilt University, Nashville, TN, USA

[6] Center for Structural Biology, Vanderbilt University, Nashville, TN, USA

[7] Department of Chemistry, Vanderbilt University, Nashville, TN, USA

[8] Department of Biomedical Sciences, Idaho College of Osteopathic Medicine, Meridian, ID, USA

[9] Computational Chemistry and Molecular Biophysics Section, NIDA, NIH, Baltimore, MD, USA

[10] Molecular Neurosciences, Developmental Neurosciences, University College London (UCL) Great Ormond Street Institute of Child Health, UCL, London, United Kingdom

[11] Laboratory of Molecular & Cellular Neurobiology, NIMH, NIH, Bethesda, MD, USA

[12] Institute for Drug Discovery, Leipzig University Medical School, Leipzig, Germany

# equal contribution

Correspondence:

Aurelio Galli

1032 Tinsley Harrison Tower, 1900 University Boulevard, Birmingham, AL 35233

agalli@uab.edu

(205) 934-1353

ABSTRACT

Parkinson disease (PD) is a progressive, neurodegenerative disorder affecting over 6.1 million people worldwide. Although the cause of PD remains unclear, studies of highly-penetrant mutations identified in early-onset familial parkinsonism have contributed to our understanding of the molecular mechanisms underlying disease pathology. Dopamine (DA) transporter (DAT) deficiency syndrome (DTDS) is a distinct type of infantile parkinsonism-dystonia that shares key clinical features with PD, including motor deficits (progressive bradykinesia, tremor, hypomimia) and altered DA neurotransmission. Here, we define structural, functional, and behavioral consequences of a Cys substitution at R445 in human DAT (hDAT R445C), identified in a patient with DTDS. We found that this R445 substitution disrupts a phylogenetically conserved intracellular (IC) network of interactions that compromise the hDAT IC gate. This is demonstrated by both Rosetta molecular modeling and fine-grained simulations using hDAT R445C, as well as EPR analysis and X-ray crystallography of the bacterial homolog leucine transporter. Notably, the disruption of this IC network of interactions supported a channel-like intermediate of hDAT and compromised hDAT function. We demonstrate that *Drosophila melanogaster* expressing hDAT R445C show impaired hDAT activity, which is associated with DA dysfunction in isolated brains and with abnormal behaviors monitored at high-speed time resolution.

We show that hDAT R445C *Drosophila* exhibit motor deficits, lack of motor coordination (i.e. flight coordination) and phenotypic heterogeneity in these behaviors that is typically associated with DTDS and PD. These behaviors are linked with altered dopaminergic signaling stemming from loss of DA neurons and decreased DA availability. We rescued flight coordination through enhanced DAT surface expression *via* the lysosomal inhibitor chloroquine. Together, these studies shed light on how a DTDS-linked DAT mutation underlies DA dysfunction and, more broadly, the clinical phenotypes shared by DTDS and PD.

INTRODUCTION

Parkinson's disease (PD) is the second-most prevalent neurodegenerative disorder, affecting 2–3% of the global population over the age of 65 (Chai and Lim, 2013). Although a vast majority of PD cases occur idiopathically and affect people over the age of 50 (late-onset), a subset of genetic mutations is associated with early-onset PD (Lill, 2016). Investigations of these highly-penetrant, inherited forms of PD have provided tremendous insights into specific molecular pathways that underlie neurodegeneration and motor deficits (Trinh and Farrer, 2013).

Mutations in the human dopamine (DA) transporter (hDAT) gene (*SLC6A3*) have been linked to a distinct type of infantile parkinsonism-dystonia, referred to as DA transporter deficiency syndrome (DTDS) (Kurian et al., 2011; Kurian et al., 2009; Ng et al., 2014). Few patients diagnosed with DTDS survive to adulthood, with a majority of patients dying in childhood or adolescence (Kurian et al., 2011; Kurian et al., 2009; Ng et al., 2014). Common to DTDS-linked DAT variants is a multifaceted loss of DAT function, which includes impaired transporter activity and decreased expression (Asjad et al., 2017; Beerepoot et al., 2016; Kurian et al., 2011; Kurian et al., 2009; Ng et al., 2014). However, the structural and functional underpinnings of these impairments, how they translate to specific behaviors, and whether they can be pharmacologically targeted remain mostly uncovered.

DTDS is a complex movement disorder typically characterized by initial infantile hyperkinesia (dyskinesia/dystonia) that progresses to a parkinsonian movement disorder (bradykinesia/tremor) (Kurian et al., 2011; Ng et al., 2014). Other characteristic clinical features include elevated levels of the DA metabolite homovanillic acid (HVA) in the cerebrospinal fluid and loss of DAT activity in the basal ganglia, as measured by single-photon emission tomography of DAT (i.e. DaTSCAN) (Kurian et al., 2011; Kurian et al., 2009; Ng et al., 2014). In DTDS, increased levels of HVA typically reflect increased DA turnover promoted by higher extracellular DA levels. This increase in DA levels likely reflects decreased DA clearance mediated either by loss of DAT activity and/or expression. Other forms of early-onset parkinsonism are also

82 associated with impaired DAT function (Hansen et al., 2014). This includes a patient with early-
83 onset parkinsonism and attention deficit hyperactivity disorder (ADHD) carrying compound
84 heterozygous missense mutations in *SLC6A3* that give rise to I321F and D421N substitutions in
85 the DAT protein (Borre et al., 2014; Hansen et al., 2014). To date, the mechanism through which
86 altered DAT function underlies parkinsonian phenotypes remains unclear.

87 The DAT is a presynaptic membrane protein that spatially and temporally regulates DA
88 neurotransmission by mediating the reuptake of DA from the synapse following vesicular release.
89 Among other roles, DA regulates cognition, emotion, motor activity, and motivation (Bjorklund and
90 Dunnett, 2007; Giros and Caron, 1993; Palmiter, 2008). Altered DA neurotransmission has been
91 implicated in several neuropsychiatric and neurological disorders, including ADHD, Autism
92 Spectrum Disorder (ASD) and PD (Bowton et al., 2010; Bowton et al., 2014; Cartier et al., 2015;
93 Chai and Lim, 2013; Hamilton et al., 2013; Meisenzahl et al., 2007; Russo and Nestler, 2013;
94 Swanson et al., 2007). Structural and molecular dynamic (MD) studies suggest that DA transport
95 occurs via an alternating access model, wherein the transporter alternates between various
96 “outward-facing” and “inward-facing” conformations (Forrest et al., 2008; Kazmier et al., 2014;
97 Krishnamurthy and Gouaux, 2012). hDAT can also form an aqueous pore (channel-like mode)
98 (Bowton et al., 2010; Bowton et al., 2014; Kahlig et al., 2005). We have shown that the frequency
99 of the hDAT channel-like mode is enhanced by both pharmacological targeting and disease-
100 associated variants (Bowton et al., 2010; Bowton et al., 2014; Kahlig et al., 2005). Key to this
101 alternating mechanism is a network of interactions occurring at the extracellular (EC) and
102 intracellular (IC) transporter face, termed EC and IC gates, respectively.

103 Recent work identified compound heterozygous missense mutations in the *SLC6A3* gene
104 in a patient who presented with classical DTDS: a mutation in one allele resulted in a R445C
105 substitution and a mutation in the second allele resulted in a R85L substitution (Ng et al., 2014).
106 Either mutation, when studied individually, has devastating effects on hDAT activity and
107 expression (Ng et al., 2014). In this study, we aimed to understand, mechanistically and

structurally, how R445C disrupts transport function, the behavioral consequence of this disruption, as well as whether we could rescue transport function and behaviors with pharmacotherapy. Of note, DAT has been shown to form both dimers as well as tetramers at the plasma membrane (Hastrup et al., 2003). Therefore, expression of both mutations in our experimental preparations would generate several combinations of hDAT oligomers, preventing the association of specific hDAT impairments and behavioral phenotypes to a specific mutation. Thus, we focused this study on the R445C mutation.

R445 is located close to the cytoplasmic end of TM9, facing the IC vestibule and is part of a conserved IC interaction network that comprises the IC gate (Khelashvili et al., 2015a; Kniazeff et al., 2008; Razavi et al., 2018; Reith et al., 2018; Shan et al., 2011). This network is thought to coordinate conformational rearrangements in DAT throughout the transport cycle (Kniazeff et al., 2008; Shan et al., 2011). Specifically, the R445-E428 salt bridge is predicted to stabilize the transition of hDAT to an inward-occluded conformation (Khelashvili et al., 2015a; Penmatsa et al., 2013; Reith et al., 2018). Previous studies showed that substitutions at R445 impair DAT function (Asjad et al., 2017; Beerepoot et al., 2016; Ng et al., 2014; Reith et al., 2018). However, how and whether R445C impacts the structure and the dynamics of the IC gate remains unclear. Importantly, how the R445C substitution contributes to DA dysfunction in disease and more specifically, DTDS etiology, is largely unknown.

Here, we undertake a close examination of the structural and functional consequences of the R445C substitution in hDAT. We integrate molecular insights from X-ray crystallography, electron paramagnetic resonance (EPR), molecular modeling, and molecular dynamic (MD) simulations to determine, mechanistically, how R445C underlies dysfunction of the DAT IC gate. Furthermore, we adopt *Drosophila melanogaster* as an animal model to examine whether and how this hDAT variant supports brain DA dysfunction, loss of DA neurons and behavioral phenotypes characterized by DTDS. Finally, we assess a pharmacological agent for its ability to rescue behavioral deficits in *Drosophila* expressing hDAT R445C. Together, this work provides

insight into the structural mechanisms underlying DAT dysfunction and the impact of DAT dysfunction on specific behaviors, as well as on the molecular mechanisms that underlie DTDS and more broadly, PD pathology.

RESULTS

hDAT R445C compromises movement vigor in *Drosophila*

Drosophila melanogaster have provided unique and critical insights on the pathogenic mechanisms underlying PD (Feany and Bender, 2000; Xiong and Yu, 2018). *Drosophila* PD models consistently recapitulate essential PD phenotypes, including neurodegeneration as well as motor and non-motor behavioral deficits (Nagoshi, 2018). In addition, mechanisms that mediate DA neurotransmission and signaling observed in other phyla are largely conserved in *Drosophila* (Yamamoto and Seto, 2014). As observed in mammals, *Drosophila* exhibit increased arousal and hyperactivity, among other stereotypies, when DAT function is altered (Brand and Perrimon, 1993; Kume et al., 2005; McClung and Hirsh, 1998).

In order to understand whether certain DAT dysfunctions are associated with specific phenotypes in *Drosophila,* we assessed whether the R445C missense mutation in the DAT promoted behaviors associated with common DTDS phenotypes. We adopted the Gal4/UAS system to express hDAT WT or hDAT R445C specifically in DA neurons of flies homozygous for the *Drosophila* DAT null allele (DAT^{fmn}) (Campbell et al., 2019; Cartier et al., 2015; Hamilton et al., 2013). This system has two parts: the Gal4 gene, encoding the yeast transcription activator protein Gal4, and the upstream activation sequence (UAS), a minimal promoter region to which Gal4 specifically binds to activate the transcription of the gene of interest (in this study, hDAT). We developed flies where Gal4 expression is driven by the tyrosine hydroxylase (TH) promoter (TH-GAL4), driving the expression of Gal4 specifically in DA neurons (in flies, octopamine, the *Drosophila* analog of norepinephrine, does not require TH for synthesis). The gene of interest is inserted into an attB donor plasmid with a UAS site (Bischof et al., 2007). This approach allows

for irreversible integration of the gene of interest into the identical genomic locus *via* an integrase (phiC31) through the integrated phage *att*achment site, *attP* (the recipient site in the Drosophila genome). This leads to expression of comparable levels of mRNA for transgenes (e.g. hDAT). These transgenic organisms are generated with no need for mapping of the insertion site (Bischof et al., 2007).

We first determined that utilizing the Gal4/UAS system to express hDAT WT specifically in DA neurons of *DAT*^{fmn} flies does not alter DA-associated phenotypes compared to wild type animals expressing *Drosophila* DAT (dDAT). To do this, we investigated whether hDAT WT, in *Drosophila* brains, could support the reverse transport (efflux) of DA evoked by amphetamine (AMPH) as observed for dDAT. The psychostimulant AMPH evokes DA efflux mediated by the DAT (Robertson et al., 2009). To measure DA efflux by amperometry, we guided a carbon fiber electrode into the *Drosophila* brain juxtaposed to the mCherry-tagged posterior inferior lateral protocerebrum (PPL1) cluster of DA neurons (see below for details) (Shekar et al., 2017) In **Supplemental Fig. 1A** (top), representative traces display current measurements of AMPH (20 µM)-induced DA efflux from this population of neurons from *DAT*^{fmn}, dDAT, and hDAT WT fly brains. Quantitation of correspondent peak currents (**Supp. Fig. 1A, bottom**) demonstrate comparable efflux for dDAT and hDAT. Cocaine (20 µM), a DAT blocker, inhibited the ability of AMPH to cause DA efflux in hDAT WT brains (**Supp. Fig. 1A, top**). Further, we determined that uptake of [^{3}H]DA in hDAT WT *Drosophila* brains was not significantly different from that measured in dDAT brains (**Supp. Fig. 1B**). The absence of uptake in the *DAT*^{fmn} fly brains shows the dependence of DA uptake on the DAT.

In *Drosophila*, locomotion is regulated by DA neurotransmission as well as DAT function (Campbell et al., 2019; Cartier et al., 2015; Hamilton et al., 2014; Hamilton et al., 2013; Pizzo et al., 2014). We have previously demonstrated that AMPH causes changes in locomotion, a behavior that depends on DAT function/expression (Cartier et al., 2015; Hamilton et al., 2014). Adult *Drosophila* males were fed a sucrose solution (5 mM) containing either AMPH (1 mM) or

vehicle (CTR). Locomotion was measured by beam crossing detection over a 60-minute period. In *Drosophila* expressing dDAT, AMPH significantly stimulates locomotion (**Supp. Fig. 1C**). Remarkably, in *DAT*^{fmn} flies, AMPH did not increase locomotion (**Supp. Fig. 1C**). These data demonstrate that in adult *Drosophila*, functional DAT is required for AMPH-induced locomotion. To support this animal model for studying how changes in hDAT function affects behaviors, we rescued AMPH-induced locomotion in the *DAT*^{fmn} flies by expressing hDAT selectively in DA neurons using the Gal4/UAS system (**Supp. Fig. 1C**). These data strongly support *Drosophila* as a model system to test the multiple functions of hDAT *in vivo*.

We tested flies for spontaneous locomotor activity and "anxiety"-related behaviors, such as time spent in or near the center of an enclosure during an open-field test (i.e., center time). Illustrated are representative trajectories of adult hDAT WT flies (**Fig. 1A**, *black trace*) and hDAT R445C flies (**Fig. 1A**, *blue trace*) assayed in an open-field test for 5-min. We observed no differences in center time in hDAT R445C flies with respect to hDAT WT flies (**Fig. 1B**; hDAT WT: 0.016 ± 0.003 (t/t_{total}); hDAT R445C: 0.024 ± 0.006 (t/t_{total}); $p > 0.05$). We did observe a significant reduction in spontaneous locomotor activity in hDAT R445C (59.7 ± 6.1 cm) compared with hDAT WT flies (80.1 ± 4.2 cm; $p = 0.008$) (**Fig. 1C**). Given that parkinsonian locomotor deficits can be characterized by hypokinesia (inability to initiate movement) and bradykinesia (slowed movement), we dissected the specific locomotor deficits observed in hDAT R445C flies. We determined the frequency with which specific velocities were explored throughout the test period (**Fig. 1D**). We defined "initiating movement" as velocity = 0.74 - 0.94 mm/s and "fast movement" as velocity = 5.3 – 10.0 mm/s and determined their frequency per genotype. hDAT R445C flies spent 5.0 ± 0.3 % of the testing period initiating movement compared with 5.2 ± 0.4 % for hDAT WT flies, suggesting hDAT R445C flies did not have difficulty performing this task ($p > 0.05$; **Fig. 1E**). In contrast, hDAT R445C flies displayed significantly decreased movement vigor, in fast movement for only 9.8 ± 1.4 % of the testing period compared with 14.5 ± 1.1 % for hDAT WT

flies ($p = 0.0098$; **Fig. 1F**). Together, these data suggest that motor deficits in hDAT R445C flies are primarily characterized by deficits in movement vigor.

hDAT R445C impairs selective coordinated movements

Patients with early-onset as well as sporadic PD often present impairments in coordination (van den Berg et al., 2000). To understand further the contribution of the DAT to coordinated motor behaviors, we analyzed a quintessential fly behavior: flight. Various monoamines, including DA, modulate insect flight (Sadaf et al., 2015). Inhibition of specific TH-positive DA neurons has been found to compromise flight, including impaired wing coordination and kinematics (Sadaf et al., 2015). Initiating voluntary flight (take-off) consists of an initial phase of wing elevation, followed by a second phase of simultaneous left- and right-wing depression and leg extension (Zabalax et al., 2008). Using a high-speed camera (2,000 fps), we quantified the time that elapsed between the initiation of wing elevation ($t = 0$) and final take-off from a water surface (**Fig. 2A** and **Supp. Movie hDAT WT**). We found that flight initiation was significantly compromised in hDAT R445C flies as the corresponding duration of take-off was 60.9 ± 8.7 ms compared with 36.6 ± 4.4 ms for hDAT WT flies ($p = 0.03$) (**Fig. 2B** and **Supp. Movie hDAT R445C**). To determine whether impairments in coordination were consistent across multiple modalities, we assessed grooming. In *Drosophila,* this stereotyped, coordinated movement of the forelegs and hindlegs is prompted by a mechanical or microbial stimulus and is modulated by dopaminergic neurotransmission (Pitmon et al., 2016). Interestingly, grooming was not significantly impaired in hDAT R445C flies (116.7 ± 12.9 s) relative to hDAT WT flies (88.8 ± 7.7 s; $p > 0.05$) (**Fig. 2C**). These data suggest that only specific coordinated movements are impaired in hDAT R445C flies.

hDAT R445C flies display DA deficiency

DA dysregulation, specifically the loss of DA signaling, drastically alters the timing, velocity and fluidity with which movement is executed (Panigrahi et al., 2015; Turner and Desmurget, 2010). We thus sought to determine whether impairments in movement and coordination were

driven by altered DA dynamics. We first measured DA content in whole brains of hDAT WT and hDAT R445C flies. DA content was significantly reduced by 16.9 ± 3.2 % in hDAT R445C (21.4 ± 0.8 ng/mg) relative to hDAT WT brains (25.8 ± 1.0 ng/mg) ($p = 0.02$) (**Fig. 3A, left**). We also measured serotonin (5-HT) content, as serotonergic dysfunction has also been associated with the development of motor and non-motor symptoms in PD (Politis and Niccolini, 2015). We found that 5-HT content was comparable in hDAT WT (67.0 ± 1.8 ng/mg) and hDAT R445C (60.7 ± 2.1 ng/mg; $p > 0.05$) brains (**Fig. 3A, right**).

Various *Drosophila* PD models have shown selective neurodegeneration of protocerebral posterior lateral 1 (PPL1) DA neurons (Barone et al., 2011; Cackovic et al., 2018; Trinh et al., 2008; Whitworth et al., 2005). These clusters of neurons, which innervate the mushroom and fan-shaped bodies, are implicated in regulating motivated behaviors as well as reward learning and reinforcement. Thus, they exhibit parallel functions compared to DA projections from the substantia nigra to the striatum in mammals (Aso et al., 2012; Berry et al., 2012; Claridge-Chang et al., 2009; Kirkhart and Scott, 2015; Riemensperger et al., 2011). We assessed the number of TH-positive PPL1 neurons in hDAT WT and hDAT R445C brains (**Fig. 3B, left**). We found TH-positive PPL1 neurons to be significantly reduced in hDAT R445C flies (9.1 ± 0.4) relative to hDAT WT controls (11.5 ± 0.2; $p < 0.0001$) (**Fig. 3B, right**). These data demonstrated that specific motor deficits are associated with DA deficiency in hDAT R445C flies.

To determine the effects of R445C on DAT function, we examined reverse transport (efflux) of DA evoked by amphetamine (AMPH) in isolated *Drosophila* brains. The psychostimulant AMPH evokes DA efflux mediated by the DAT. To measure DA efflux, we utilized amperometry in isolated *Drosophila* brains. We guided a carbon fiber electrode into the brain, juxtaposed to the mCherry-tagged PPL1 DA neurons (Shekar et al., 2017) (**Fig. 3C, left, red box**). The representative traces displayed are amperometric current measurements of DA efflux from this population of neurons in hDAT WT and hDAT R445C brains (**Fig. 3C, middle**). Given

the DA deficiency in hDAT R445C brains, it was not surprising that AMPH-induced DA efflux was significantly reduced in hDAT R445C (0.76 ± 0.14 pA) compared with hDAT WT (1.74 ± 0.37 pA; p = 0.04) brains. Nonetheless, these brains were capable of DA efflux, suggesting that hDAT R445C can support, at least in part, the reverse transport of DA.

Substitutions in LeuT, at the site homologous to R445 in hDAT, disrupt IC network interactions

LeuT, the bacterial homolog of hDAT, has provided key insights that have improved our understanding of Na^+/substrate-coupled transport in the neurotransmitter sodium symporter (NSS) family (Beuming et al., 2006; Yamashita et al., 2005). Integrating data from LeuT crystal structures, electron paramagnetic resonance (EPR), single-molecule fluorescence energy transfer (sm-FRET) and MD simulations has defined the alternating access mechanism used by the NSS family to transport substrate. Common to these models is the transition from outward-facing open (OF) to inward-facing open (IF) states through the opening and closing of the EC and IC gates, respectively (Claxton et al., 2010; Kazmier et al., 2014). Here, we use a combination of Rosetta modeling, X-ray crystallography and EPR spectroscopy to determine the consequence of hDAT mutations at R445 on conformational changes in LeuT.

Previous studies of LeuT conformational dynamics have shown that the network of interactions between the N-terminus (residues R5, E6, W8), TM6/IL3 (Y265, Y268), TM8 (D369) and TM9 (R375) are key to occluding the IC vestibule in the outward-facing occluded (OO) state (Cheng and Bahar, 2014). In particular, salt bridges R5-D369 and E6-R375 stabilize the N-terminus in the OO state, as illustrated in **Fig. 4A** (**left**). The residues participating in this network are highly conserved across the NSS family, and are thus, likely critical to transport. First, we determined the effects of substitutions at the LeuT residue corresponding to R445 of hDAT, R375 in LeuT: LeuT R375A, LeuT R375D, and LeuT R375C. We constructed molecular models of LeuT R375A and R375D (**Fig. 4A**) using Rosetta to determine potential changes in these interactions and in the thermodynamic stability (ΔΔG) of these variants relative to WT. We found

that both neutralizing and acidic substitutions at R375 likely promote the dissociation of the E6-R375 salt bridge (closest atom-atom distances: WT= 2.1 Å; R375A = 5.4 Å; R375D = 4.2 Å), weaken the interaction of R375 and I184 (closest atom-atom distances: WT = 2.5 Å; R375A = 6.0 Å; R375D = 4.7 Å), and decrease the thermodynamic stability of LeuT (Rosetta scores: R375A = + 4.4 REU; R375D = + 5.6 REU relative to WT) (**Supp. Fig. 2A - B, Fig. 4A**). Other interactions were largely preserved, including R5-D369 and E6-I187 interactions (**Fig. 4A**). One difference between these models was that K189 moved towards E6 in LeuT R375A, but away from E6 in LeuT R375D (**Supp. Fig. 2A**). Together, these models predicted that both acidic and neutral mutations at the LeuT counterpart (R375) of hDAT R445 disrupt the interactions near the IC vestibule, partially affecting the IC gate, but maintaining other IC network interactions. We also generated a model for LeuT R375C, and found that K189 also moves away from E6. We conclude that a cysteine mutation at R375 more closely resembles an acidic substitution (compare **Fig. 4A** and **Supp. Fig. 2A, C**). However, it has to be noted that cysteine residues exist at an equal ratio of protonated (neutral) to deprotonated (acidic) states at physiological pH. The root-mean-square deviation (RMSD) was calculated to show the correlation between the energy-optimized models and the experimental model (**Supp. Fig. 2D**).

To define further the structural consequences of R375 substitutions, we determined the X-ray crystal structures of LeuT WT, LeuT R375A and LeuT R375D solved in the L-Ala and Na^+ bound OO conformation to a resolution of 2.1 Å for WT and R375A, and 2.6 Å for R375D (**Fig. 4B,** detailed in **Supp. Fig 3**). Unfortunately, the expression of the R375C mutant was low and protein yield was insufficient for crystallography. Structures were aligned with a previous structure of LeuT WT in an OO conformation (PDB ID: 3F3E) with an RMSD of 0.134, 0.146 and 0.236 for LeuT WT, R375A and R375D, respectively. In all structures (*superimposed*), L-Ala, Na1 and Na2 (*purple spheres*) could be modeled into their respective binding sites (**Fig. 4B, left**). These crystal structures showed that R375A and R375D substitutions in LeuT (**Fig. 4B**) precluded salt bridge formation between R375 and E6, and between R375 and the backbone of I184 as was also

observed with Rosetta modeling in **Fig. 4A**. In addition, K189 moved towards E6 by 3.4 Å, reducing the distance between residues K189 and E6 from 8.0 Å in LeuT WT to 4.6 Å in LeuT R375A (**Fig. 4B, middle bottom**), in agreement with Rosetta modeling. The distance between residues R5 and D369, and between residues E6 and I187, was conserved in all three structures (**Fig. 4B, right bottom**), as also found with Rosetta modeling (**Fig. 4A)**. As evident from these data, as well as the REU versus RMSD plots (**Supp. Fig. 2D**), our Rosetta models parallel our crystal structures. In addition, these data indicate that the IC gate is disrupted by substitutions at position R375 as a result of molecular rearrangements more complex than previously hypothesized (Reith et al., 2018).

R375 substitutions disrupt alternating access in LeuT

To monitor impact of R375 substitution on the ligand-dependent conformational dynamics of the EC and IC gates, we used EPR, and more specifically, double electron-electron resonance (DEER), to obtain distance distributions between spin label pairs 309/480 and 7/86 (**Fig. 5A, left and right, respectively**). These spin label pairs are used to monitor the isomerization of LeuT between the OF, OO, IF and inward-facing occluded (IO) states, as previously described (Campbell et al., 2019; McHaourab et al., 2011). It is important to note that the spin labels were attached at introduced cysteines, hence precluding the investigation of LeuT R375C. Instead, we monitored the effects of R375A and R375D substitutions on LeuT conformational dynamics. We found that these substitutions had relatively minor effects on the EC gate (309/480 pair). In the absence of ion and substrate (Apo), LeuT WT dwells between OO and OF conformation, with OO being predominant (**Fig. 5B, left**; *black trace*). Na^+ enhances the OF conformation poised to bind substrate (**Fig. 5B, left**; *red trace*) (Claxton et al., 2010). Leu binding to Na^+-bound LeuT restores the conformational preference to the OO form (**Fig. 5B, left;** *blue trace*). We found that the introduction of an Ala (**Fig. 5C, left**) or Asp (**Fig. 5D, left**) at position R375 did not drastically affect the EC gate in the Na^+/Leu intermediate (*blue trace*) but, longer-distance components are sampled in the Apo (*black trace) and* Na^+ *(red trace)* forms. In R375D, the probability distribution

of the dominant short-distance component (OO) decreased, such that more open intermediate distances were sampled in the Apo state (*black trace*) (**Fig. 5D, left**).

More substantial changes were observed on the IC gate. Consistent with previous findings, the spin label pair monitoring of the IC gate in LeuT WT showed a bimodal distribution between IF and IO conformations in the Apo state (*black trace*), whereas Na^+ alone (*red trace*) begins, and Na^+/Leu (*blue trace*) completes, biasing LeuT towards the IO conformer (**Fig. 5B, right**). The substitution R375A increased the probability of an IF conformation only in the Apo (*black trace*) and Na^+/Leu states (*blue trace*) (**Fig. 5C, right**). Similarly, R375D suppressed the short-distance component (IO conformation) in favor of an IF conformation in the Apo state (*black trace*) (**Fig. 5D, right**). The addition of Na^+ was able to partially rescue the probability distribution of the IO conformer, where Na^+/Leu resets the IC gate to the IO conformation (**Fig. 5D, right**).

Together, DEER distance distributions demonstrate that the substitution of R375D leads to increased probability of open conformations on both sides of the transporter. This may suggest the population of a channel-like state consistent with the prediction from MD simulations described below.

R445 substitutions lead to the intermittent formation of a channel-like intermediate in hDAT

To determine the structural and dynamic changes induced by a R445C substitution in hDAT, we generated homology models of hDAT based on dDAT structures (PDB ID: 4M48). As illustrated in **Fig. 6A**, salt-bridges at the IC surface (e.g. R445-E428 and R60-D436), a cation-π interaction between R60 and Y335, and a hydrogen bond between E428 and Y335, form an IC network of interactions that stabilizes the occlusion of the IC vestibule in hDAT WT (**Fig. 6A**) (Cheng and Bahar, 2015; Kniazeff et al., 2008; Shan et al., 2011). *In silico* studies have suggested that disruption or reconfiguration of these IC salt bridges facilitate the opening of the IC vestibule for release of substrate or ions (Cheng and Bahar, 2015; Khelashvili et al., 2015b). This feature has also been noted in the human serotonin transporter (hSERT) in recent cryo-EM structures (Cheng and Bahar, 2019; Coleman et al., 2019).

The structural model generated for hDAT R445C showed that this substitution disrupts this IC interaction network to support an intermittent channel-like intermediate (**Fig. 6B**) which is characterized by continuous water occupancy in the transporter lumen. Superposition of hDAT WT and R445C structures (**Fig. 6C**) showed an overall opening of the transmembrane (TM) helices on the IC face (TM9, *blue arrow*) in hDAT R445C. MD simulations also showed that Na^+ migrates from either the IC or EC side (**Fig. 6D**), where Na^+ binding occurs prior to the complete dissociation of R60-D436 salt bridge at 150 ns that is paralleled by the formation of the new E428-R60 salt bridge (**Fig. 6E**). We also note that the IC-exposed TM1a-TM6b pair retained their 'closed' state (**Fig. 6F**), in contrast to the usual opening of TM1a in the IF state observed in WT. Finally, Na^+ entry was facilitated by the opening of TM9 and consequent increase in the interhelical distance between TM9 and TM6b (**Fig. 6F**).

Similar channel-like intermediates were observed in hDAT R445A (data not shown) and R445D (**Supp. Fig. 4A**). In R445D, three Na^+ ions (*cyan, violent and orange spheres*) stabilize along the solvated transporter lumen: one entering from the IC region, one entering from the EC region, and one intermittently diffusing from the IC region (**Supp. Fig. 4B**). In contrast, only two Na^+ binding sites are present in R445C (**Fig. 6B**). It is likely that the dissociation of the R445-E428 salt bridge promoted by R445D substitution allows E428 to bind an additional Na^+. In contrast, in hDAT R445C, E428 finds an alternative partner, R60. These findings point to a unique feature of the R445 residue, as substitutions associated with DTDS stabilize a channel-like conformation only observed occasionally in previous simulations (Cheng et al., 2018).

We also observe that the dissolution of the R445-E428 salt-bridge weakened the IC interaction network as a whole. In particular, R445C weakened the association of TM8-TM9 near the IC entrance, whereby TM9 underwent an outward tilting exposing an egress pathway along TM8 for Na^+ (or a different cation) (**Fig. 6C**). The outward titling of TM9 has been observed previously in the DA-loaded transition from OF to IO states (Cheng and Bahar, 2015). Furthermore, R455C substitution increases the likelihood that the R60-D436 salt bridge breaks,

while promoting the formation of a new salt bridge R60-E428 (**Fig. 6E**) at the expense of breaking R60-D436 salt-bridge in both runs. This new salt bridge may lock the IC gate in a new configuration.

hDAT R445C displays reduced expression that is partially rescued by chloroquine

hDAT R445C isolated brains display a reduction in DA content (**Fig. 3A**). Thus, we determined the expression of hDAT R445C in a heterologous expression system. R445C substitution reduced the surface expression to 0.06 ± 0.01 of hDAT WT (1.0 ± 0.04; $p < 0.0001$) and the total mature DAT expression to 0.20 ± 0.04 of hDAT WT (marked by #; 1.0 ± 0.05; $p < 0.0001$) (**Fig. 7A**). Given this reduction in transporter expression, in addition to structural rearrangements, we suspected that DA uptake would also be impaired. Indeed, [^{3}H]DA uptake kinetics showed that R445C expressing cells have significantly reduced transport capacity with respect to WT cells, as reflected in the V_{max} ($F_{(1, 15)} = 160.3$; $p < 0.0001$) (**Fig. 7B**). However, the apparent affinity for DA (K_m) significantly increased in hDAT R445C relative to WT ($p < 0.0001$) cells, suggesting that conformational changes required for translocation of DA across the membrane are also affected (**Fig. 7B**). To determine if R445C affected the reverse transport function of the DAT (DA efflux), we delivered DA (2 mM for 10 min) to the inside of the cell through a patch-pipette in whole-cell configuration and used amperometry to measure DA efflux in response to AMPH (10 μM) (Belovich et al., 2019). Thus, we were able to load the cells with equal concentrations of DA despite differences in DA uptake. Consistent with our *ex vivo* brain amperometric recordings, we found that R445C supported DA efflux, albeit significantly reduced compared with WT (hDAT WT = 0.74 ± 0.09 pA; hDAT R445C = 0.28 ± 0.06 pA; $p = 0.001$) (**Fig. 7C**).

We also found that both neutralizing and anionic substitutions at R445 (hDAT R445A and hDAT R445D) significantly compromised surface DAT ($p < 0.0001$) and mature DAT expression ($p < 0.0001$) relative to hDAT WT (**Supp. Fig. 5A, Supp. Fig. 6A**). In agreement with this reduction

in hDAT surface expression and observed structuralimpairment, [^{3}H]DA uptake was also significantly reduced in hDAT R445A ($F_{(5,92)}$ = 22.7, p < 0.0001; **Supp. Fig. 5B)** and hDAT R445D expressing cells ($F_{(5,94)}$ = 42.1; **Supp. Fig. 6B**). Consistent with data from the R445C mutant, we find that the K_m of hDAT R445A and hDAT R445D was also significantly increased. Combining patch-clamp with amperometry (as above), we found that AMPH-induced DA efflux was significantly compromised in hDAT R445D (p = 0.002; **Supp. Fig. 6C**) compared with hDAT WT cells. Interestingly, we observed that AMPH caused a reduction in the amperometric current in hDAT R445A compared with hDAT WT cells (p = 0.001; **Supp. Fig. 5C**), consistent with AMPH blocking constitutive DA efflux, as previously noted in other DAT mutations (Bowton et al., 2010; Mazei-Robison et al., 2008). Together, these data confirm that substitutions at R445 significantly compromised DAT cell surface expression and function.

The severity and onset of clinical phenotypes are associated with residual DAT function in DTDS (Kurian et al., 2011; Ng et al., 2014). DAT function is related to its expression in hDAT R445C and other DTDS-associated variants; thus, we assessed the possibility of improving motor coordination deficits in hDAT R445C flies by enhancing/correcting DAT expression. DAT expression and degradation are regulated by endocytic, recycling, and lysosomal pathways (Daniels and Amara, 1999; Loder and Melikian, 2003; Miranda et al., 2007; Wu et al., 2015). Previous studies have shown that chloroquine (CQ), a lysosomotropic weak base that inhibits lysosomal activity, limits DAT lysosomal degradation (Cartier et al., 2019; Daniels and Amara, 1999). In DTDS-associated variants, the ratio of mature (glycosylated; mDAT) to immature (unglycosylated; iDAT) DAT is shifted where the immature form predominates (**Fig. 7A**) (Kurian et al., 2011), suggesting DAT degradation. Here, we investigated whether inhibition of DAT lysosomal degradation using CQ could improve this ratio. We found that CQ treatment (1 mM, 4 h) significantly increased the ratio of mature DAT (marked by #) to immature DAT (marked by *) in hDAT WT (vehicle: 1.0 ± 0.07; CQ: 1.4 ± 0.06; p = 0.04) as well as in hDAT R445C expressing cells (vehicle: 1.0 ± 0.1; CQ: 1.6 ± 0.1; p = 0.003) ($F_{(1,20)}$ = 18.0) (**Fig. 7D**). As specified above in

DTDS, the severity of clinical phenotypes is correlated with DAT function/expression. Thus, we sought to determine whether the improvement in DAT expression promoted by CQ translated to improvements in motor phenotypes. We supplemented fly food with either CQ (3 mM, 72 h) or vehicle for both hDAT WT and hDAT R445C flies and measured the timing of flight initiation. We found that CQ treatment significantly improved the time for flight initiation in hDAT R445C flies relative to vehicle ($F_{(1,29)}$ = 8.7, p = 0.04) (**Fig. 7E**). CQ did not have significant effects on motor coordination in hDAT WT flies (p > 0.05). These data suggest that CQ, by enhancing DAT expression, can improve flight initiation in hDAT R445C flies, and that when a threshold level of DAT expression is achieved, further increases in DAT expression do not enhance flight initiation time.

DISCUSSION

PD is a multi-system, heterogenous neurodegenerative disorder characterized clinically by core motor symptoms including resting tremors, bradykinesia, rigidity and postural instability. As the disease progresses, additional motor symptoms develop, such as impairments in gait and balance, eye movement control, speech and swallowing, and bladder control. Mood disorders (e.g. anxiety and depression), sleep disorders (e.g. insomnia, disrupted circadian rhythm), hyposmia (impaired olfaction), gastrointestinal symptoms and other non-motor features usually precede full PD diagnosis (Faivre et al., 2019). Additionally, cognitive impairment, including dementia, typically manifests after diagnosis and progresses steadily over time (McGregor and Nelson, 2019). Some motor and behavioral symptoms can be alleviated by DA replacement therapies, such as levodopa (L-DOPA, a DA precursor), DA metabolism inhibitors and DA receptor agonists (Jenner, 2015). However, as the disease progresses, there is often a “loss of drug” effect, with symptoms largely refractory to therapeutic interventions (Jenner, 2015). In some patients, DA replacement can promote new behavioral phenotypes, most commonly: impulse control disorder (ICD) and DA dysregulation syndrome (DDS). In ICD, patients impulsively or

compulsively engage in reward-seeking behaviors, including gambling, eating, or sexual activities (Weintraub et al., 2010). In DDS, patients display addictive behaviors with dependence or withdrawal-type symptoms towards their DA medications (Giovannoni et al., 2000). Essential to developing new pharmacotherapies is understanding the underlying disease pathology.

Although the cause of PD is not completely understood, a combination of aging, neuronal susceptibility, genetic risks and environmental factors have been found to contribute its etiology. Studies on highly-penetrant mutations identified in familial parkinsonism, as well as candidate gene and genome-wide association findings in idiopathic PD, have contributed to our understanding of the molecular mechanisms underlying disease pathology (Trinh and Farrer, 2013). DTDS is a distinct type of infantile parkinsonism-dystonia associated with DAT dysfunction that shares various clinical phenotypes with PD, including motor deficits and altered DA homeostasis (Kurian et al., 2011; Kurian et al., 2009; Ng et al., 2014). Investigations on DTDS-associated DAT variants are essential to understanding the impact of DAT dysfunction on DA neurocircuits and signaling pathways. Further, these studies may shed light on the molecular mechanisms that underlie the clinical phenotypes shared by DTDS and PD (Mou et al., 2019).

In this study, we define how a specific DAT variant identified in DTDS (R445C) confers DAT dysfunction as well as impairments in DA neurotransmission and associated behaviors. R445C alters the structure and gating dynamics of an IC interaction network as well as DAT expression. In the NSS superfamily, which includes DAT and LeuT, thermodynamic coupling of substrate and Na^+-co-transport occurs via an alternating access mechanism that comprises the opening and closing of the IC and EC gates (Beuming et al., 2006; Yamashita et al., 2005). R445 is aligned to R375 in LeuT, which forms the R375-E6 salt-bridge as part of the IC gate (Cheng and Bahar, 2014). Our crystallographic data, supported by modeling and $\Delta\Delta G$ calculations in LeuT, revealed that substitutions at R375 in LeuT disrupt key IC interactions, including the R375-E6 salt-bridge, promoting an IF conformation.

These findings are consistent with previous *in silico* studies which suggest that the transition to an IF conformation is defined by the dissolution of IC salt-bridges D369-R5 and R375-E6 in LeuT (Cheng and Bahar, 2014). Furthermore, from our EPR studies, we surmise that R375 substitutions disrupt the IC network and bias LeuT to an IF conformation, subsequently altering transport, which requires LeuT to isomerize toward an OF conformation. We have previously shown that other mutations associated with neuropsychiatric disorders (i.e. ΔV269) that disrupt this IC network also bias LeuT to an IF conformer, impairing transporter function (Campbell et al., 2019). It is important to note that in the Apo conformation R375A does not alter LeuT IC gate to the extent of R375D. This suggests that some variants at this site are more tolerated, likely due to nearby residues conferring redundant interactions to this IC interaction network. Indeed, it has been previously noted that the microenvironment surrounding the IC gate is enriched with putative interaction partners that reinforce this IC network (Kniazeff et al., 2008). Finally, in the EC gate, R375A promotes longer-distance components sampled in the Apo, Na^+ and Na^+/Leu states.

Using homology modeling and MD simulations, we were able to uncover the structural and dynamic changes induced by the R445C mutation in hDAT. In hDAT, R445 forms a salt bridge with E428, an association that is highly conserved among several eukaryotic NSS members and is proposed to be part of the IC gate (Reith et al., 2018). Although this association is distinct from the R375-E6 salt-bridge in LeuT, it is thought to serve similar functions as part of the IC network. We found that R445C promotes the dissociation of salt-bridge R445-E428, as previously predicted by Reith and collaborators by using molecular graphics (Reith et al., 2018). However, our MD simulations demonstrate that, unexpectedly, the R445C mutation also disrupts the R60-D436 salt bridge and induces intermittent formation of a new salt bridge, E428-R60. These rearrangements of the IC network give rise to a channel-like intermediate filled with water molecules. This channel-like intermediate was also observed in hDAT R445D, with an additional Na^+ binding the transporter from the IC environment. Previous studies have shown that DAT

519 undergoes uncoupled DAT-mediated ionic fluxes (Ingram et al., 2002), as well as reverse
520 transport of DA (efflux), via channel-like pathways (Kahlig et al., 2005). We have previously
521 uncovered that the hDAT coding variant A559V, identified in patients with ADHD, supports a
522 channel-like mode in DAT which is associated with persistent DAT-mediated reverse transport of
523 DA (DA leak) uncovered by AMPH blockade (Bowton et al., 2014; Mazei-Robison et al., 2008).
524 This DA leak was also identified in hDAT T356M, a *de novo* missense mutation in ASD (Hamilton
525 et al., 2013). We conclude that the channel-like intermediate observed in our simulations of R445
526 substitutions may be associated with a channel-like mode supporting ion fluxes. Interestingly, we
527 found that a neutral substitution at R445 (hDAT R445A) results in constitutive, anomalous DA
528 leak blocked by AMPH. These data highlight the possibility that anomalous DA efflux may
529 increase risk for various psychiatric disorders (Bowton et al., 2010; Hamilton et al., 2013; Hansen
530 et al., 2014; Mazei-Robison et al., 2008). It is important to note that constitutive DA efflux is not
531 observed in cells expressing hDAT R445C nor hDAT R445D. This underscores the complexity of
532 the IC network and the possibility that distinct amino acid substitutions at R445 differentially affect
533 the IC dynamics, promoting different hDAT functions.

534 Our *in vitro* analysis, combined with our *in silico* data, revealed that impaired DAT R445C
535 transport capacity stems both from a reduction in transporter expression as well as impaired hDAT
536 function that reflects compromised DA uptake, but partially supported DA efflux. Our findings are
537 consistent with previous studies highlighting impaired transporter expression and uptake in hDAT
538 R445C cells (Asjad et al., 2017; Beerepoot et al., 2016; Ng et al., 2014). In addition, these data
539 support the idea that the IC gate differentially regulates inward versus outward transport of DA
540 (Campbell et al., 2019), as R445C supports DA efflux (albeit reduced). In addition, we find that
541 specific substitutions at this IC interaction network are distinctly tolerated in LeuT versus hDAT,
542 as has been previously noted with other substitutions at this site (Stolzenberg et al., 2015). In
543 hDAT, neither neutral (R445A) nor acidic (R445D) substitutions support normal hDAT function.
544 These findings contrast EPR measurements, which suggest that neutral (R375A) but not acidic

(R375D) substitutions are tolerated in LeuT. These findings highlight key differences in the IC and perhaps redundancy existing in LeuT within this network that is absent in the hDAT.

Despite neuroanatomical differences between mammalian and fly brains, increasing evidence on the evolutionary relationships between molecules, neural networks and organization within mammalian and invertebrate brains, as well as studies on animal models of disease, suggest many similarities (Anderson and Adolphs, 2014; Feany and Bender, 2000; Hartenstein and Stollewerk, 2015; Kaiser, 2015; Nagoshi, 2018; Xiong and Yu, 2018; Yamamoto and Seto, 2014). We used *Drosophila* as an animal model to explore the physiological and phenotypic consequences of a cysteine substitution at R445 of DAT. Our studies found that hDAT R445C promotes altered motor and coordinated behaviors in *Drosophila*. Specifically, hDAT R445C *Drosophila* displayed impaired locomotion that was driven by compromised movement vigor (fast movement). This behavioral phenotype is parallel to bradykinesia observed in patients with DTDS and PD (Chai and Lim, 2013; Kurian et al., 2011; Kurian et al., 2009; Ng et al., 2014) as well as in various mammalian and *Drosophila* models of PD (Feany and Bender, 2000; Nagoshi, 2018; Taylor et al., 2010).

In patients with PD, loss of DA neurons elicits impaired movement and motor symptoms, as well as compromised fine and gross motor coordination. In flies, flight initiation requires exquisite sensory-motor integration. A fly first raises its wings to a ready position, and then subsequently, extends its mesothoracic legs and depresses its wings simultaneously to coordinate a jump with the initial downstroke (Card and Dickinson, 2008). Here, using a high-speed camera, we studied flight initiation in a *Drosophila* model of DTDS to understand the effects of hDAT R445C on sensory-motor integration. We found spontaneous flight initiation to be significantly delayed in *Drosophila* expressing hDAT R445C. Similarly, recent studies have observed wing coordination defects in flies with reduced neurotransmitter release from DAergic neurons (Sadaf et al., 2015). These data suggest that there may be a reduction in DA tone in hDAT R445C flies that contributes to flight deficits. In addition, we found a disparate repetitive

motor behavior that requires fine-motor coordination, grooming, to be unaffected in hDAT R445C *Drosophila.* These findings point to the phenotypic heterogeneity commonly observed in DTDS and PD (Faivre et al., 2019; Kurian et al., 2011; Kurian et al., 2009; Lill, 2016; Ng et al., 2014; Trinh and Farrer, 2013) and suggest that specific coordinated movements are impaired or alternatively, may present in a progressive nature in this model of DTDS. It is important to note that this study focused on the motor symptoms exhibited in DTDS and PD. However, whether and if R445C promotes non-motor deficits, including cognitive impairment and hyposmia, has not been explored.

Our studies in fly brains also demonstrate that the hDAT R445C mutation drives decreased transporter function (i.e. DA efflux), impaired DA synthesis and reduced TH-labeled DA neurons. Our findings of diminished transporter function align with our previous *in vitro* findings showing reduced hDAT R445C expression (Ng et al., 2014). In PD, core motor deficits are ascribed to the loss of DA neurons in the substantia nigra and their projections to the striatum (Trinh and Farrer, 2013). To date, neurodegeneration in DTDS has not been studied in depth; however, given that affected individuals develop parkinsonism-dystonia, including resting and acting tremor, difficulty initiating movements, bradykinesia and rigidity, it is likely that DA circuits are affected. To this end, we observed a reduction in TH-labeled DA neurons in hDAT R445C flies, consistent with various *Drosophila* models of PD that show selective neurodegeneration of protocerebral posterior lateral 1 (PPL1) DA neurons (Barone et al., 2011; Cackovic et al., 2018; Trinh et al., 2008; Whitworth et al., 2005). Although these findings suggest neurodegeneration in PPL1 neurons, given the reduction in measured DA levels, it is also possible that there is an overall reduction in TH, which limits the labeling of this neuronal population. However, our behavioral data point to a decrease in DA function, as observed in PD.

Together, these findings support a mechanism where reduced DAT-mediated DA reuptake results in excessive EC dopamine and depleted presynaptic stores. Synaptic hyperdopaminergia leads to overstimulation of presynaptic D_2 autoreceptors which suppress DA

release and down-regulate tyrosine hydroxylase (TH), the rate limiting enzyme in DA synthesis, thereby, decreasing DA synthesis (Ford, 2014). This mechanism aligns with previous findings in DAT knockout animals and those with compromised DAT function (DiCarlo et al., 2019; Jones et al., 1999; Salvatore et al., 2016).

DTDS presents in a phenotypic continuum, where clinical phenotypes appear to be associated with varied, residual DAT function. Thus, higher residual DAT activity is suggested to reduce symptom severity and/or postpone the age of disease onset (Kurian et al., 2011; Ng et al., 2014). Previous studies have used pharmacological chaperones that stabilize the DAT in an IF conformation to rescue transporter expression (Asjad et al., 2017; Beerepoot et al., 2016; Ng et al., 2014). hDAT R445C function was not consistently rescued with these agents (Asjad et al., 2017; Beerepoot et al., 2016), in alignment with our EPR and *in silico* data, which showed that hDAT R445C can isomerize and is even biased toward the IF conformer. In light of previous studies which showed that CQ inhibits DAT lysosomal degradation (Cartier et al., 2019; Daniels and Amara, 1999), we tested CQ for its ability to improve motor deficits in hDAT R445C flies. We found that CQ was able to increase motor coordination in hDAT R445C flies, reducing the time to initiate flight significantly. This improvement in flight coordination was associated with improved DAT expression. It is important to note that in some studies, lysosomal dysfunction has been associated with PD (Chai and Lim, 2013; Trinh and Farrer, 2013). In these instances, lysosomotropic agents should not be considered, as they may exacerbate disease progression. In addition, although CQ and other quinines have been used for more than 400 years to treat malaria and more recently, re-purposed to treat cancer, these agents are not without substantial adverse side effects (Achan et al., 2011; Weyerhauser et al., 2018). Thus, the use of lysosomotropic agents, such as CQ, should be considered as therapeutic agents to ameliorate motor deficits only in specific cases of DTDS.

Our study reveals how a specific DAT variant identified in DTDS contributes to DAT dysfunction and subsequently, how DAT dysfunction supports altered DA neurotransmission as

well as behaviors in *Drosophila*. Moreover, this experimental paradigm supports *Drosophila* as a model system in the study of DTDS, and PD, more broadly. Our investigation on hDAT R445C provides a blueprint to gain valuable insights into the mechanisms regulating transporter function, gating and expression, and how dysfunction of these processes translates to abnormal DA physiology and behaviors.

METHODS

Cell culture: peGFP expression vector was engineered to contain synhDAT WT (hDAT WT), hDAT R445C, hDAT R445D and hDAT R445A. All vectors were sequenced via Sanger sequencing to confirm mutations. Vector DNA was transiently transfected into human embryonic kidney (HEK) cells using Fugene-6 (Roche Molecular Biochemicals) transfection reagent. eGFP (enhanced green fluorescence protein) was used for cell selection and quantitation of transfection efficiency. Cells were maintained in a 5% CO_2 incubator at 37°C in Dulbecco's Modified Eagle Medium (DMEM) supplemented with 10% fetal bovine serum (FBS), 1 mM L-glutamine, 100 U/mL penicillin, and 100 µg/mL streptomycin. All assays were conducted ~48 h post transfection.

[^{3}H] DA uptake assays: For DA uptake in a heterologous expression system: Cells were washed in KRH buffer composed of (in mM): 130 NaCl, 25 HEPES, 4.8 KCl, 1.2 KH_2PO_4, 1.1 $MgSO_4$, 2.2 $CaCl_2$, 10 d-glucose, 1.0 ascorbic acid, 0.1 pargyline, and 1.0 tropolone. KRH was titrated to pH 7.3 - 7.4. Cells were equilibrated in KRH at 37°C for 5 min. Saturation kinetics of DA were measured by incubating cells in a range of 0.1 to 15 µM DA, comprised of a mixture of [^{3}H]DA (PerkinElmer Life Sciences, Waltham, MA) and unlabeled DA. Uptake was terminated after 10 min by washing cells twice in ice-cold KRH buffer. Nonspecific binding was measured in the presence of 10 µM cocaine. K_m and V_{max} values were derived by fitting Michaelis-Menten kinetics to specific binding data. For DA uptake in dissected *Drosophila* brains: 2–5 day old males were collected, anesthetized with CO_2, and brains were dissected in Schneider's medium (GIBCO) with 1.5% BSA. The retina was removed, and four brains per condition were pooled in Millipore Millicell

649 inserts in 24 well plates. Brains were washed with Schneider's medium, then washed in a standard
650 fly saline solution (HL3) plus 1.5% BSA and 10 mM $MgSO_4$. For 15 min at room temperature,
651 brains were exposed to 200 nM [^{3}H]DA in HL3 plus 1.5% BSA and 115 µM ascorbic acid. Brains
652 were then washed six times with 1.4 mL HL3 plus 1.5% BSA at 4 °C. Brains were placed into
653 scintillation vials in 100 µL 0.1% SDS. Scintillation fluid was added to count [^{3}H]DA. Nonspecific
654 binding was measured in the presence of 20 µM cocaine.
655 **Amperometry and patch-clamp electrophysiology:** Cells were washed twice with 37°C Lub's
656 external solution composed of (in mM): 130 NaCl, 1.5 $CaCl_2$, 0.5 $MgSO_4$, 1.3 KH_2PO_4, 10 HEPES
657 and 34 d-glucose (pH 7.3 - 7.4; 300-310 mOsms/L). To intracellularly load DA, a programmable
658 puller (Model: P-2000; Sutter Instruments; Novato, CA) was used to fabricate quartz patch-
659 pipettes with a resistance of 3-8 mΩ. Pipettes were filled with an internal solution containing (in
660 mM): 110 KCl, 10 $NaCl_2$, 2 $MgCl_2$, 0.1 $CaCl_2$, 1.1 EGTA, 10 HEPES, 30 d-glucose and 2.0 DA
661 (pH 7.3 - 7.4; 280-290 mOsms/L). Upon gaining whole-cell access, the internal solution was
662 allowed to diffuse for 10 min. To record DA efflux, a carbon fiber electrode was juxtaposed to the
663 plasma membrane of the cell and held at +600 mV. After establishing a baseline, 10 µM AMPH
664 was added to the bath. Amperometric currents were low pass filtered at 1 Hz (Model: 3382; Krohn-
665 Hite Corporation; Brockton, MA), sampled at 100 Hz (Model: Axopatch 200B; Molecular Devices;
666 San Jose, CA), and analyzed off-line using pCLAMP 9 software (Molecular Devices). DA efflux
667 was quantified as the peak of the amperometric current.
668 **Biotinylation assays:** Cells were washed on ice with 4 °C phosphate-buffered saline (PBS)
669 supplemented with 0.9 mM $CaCl_2$ and 0.49 mM $MgCl_2$. Cells were incubated in 1.0 mg/ml
670 sulfosuccinimidyl-2-(biotinamido)ethyl-1,3-dithiopropionate-biotin (sulfo-NHS-SS-biotin; Pierce,
671 Rockford, IL) in PBS for 20 min at 4 °C. Excess biotin was quenched by incubating cells in 100
672 mM glycine in PBS for 15 min. Cells were solubilized in radioimmunoprecipitation assay buffer
673 (RIPA) composed of 150 mM NaCl, 1.0% NP-40, 0.5% Sodium Deoxycholate, 0.1% SDS , 50
674 mM Tris, 1 mM EDTA, 1 mM EGTA, 1 mM PMSF and protease inhibitors (1:100), and titrated to

675 pH 7.4. Cellular extracts were centrifuged for 30 min at 16,000 × g at 4 °C. The supernatant was
676 added to immunopure immobilized streptavidin beads (Pierce Chemical Company; Rockford, IL)
677 and incubated overnight at 4 °C. Beads were extensively washed and eluted in sample buffer.
678 Samples were processed according to a standard western blot protocol (see below).
679 **Western blotting protocol:** Cells were incubated in vehicle or 1 mM chloroquine (CQ) for 4 h.
680 Cells were solubilized in RIPA, sonicated and centrifuged. Supernatants were denatured in
681 sample buffer, run on SDS-PAGE gel and transferred to polyvinylidene fluoride membrane
682 (PVDF) (Millipore, Bedford, MA). Membranes were immunoblotted for DAT (1:1000) (MAB369;
683 Millipore), β-actin (1:5000) (A5441; Sigma-Aldrich; St. Louis, MO), and Na-K ATPase (1:100;
684 Developmental Studies Hybridoma Bank (DSHB), Iowa City, Iowa). The secondary antibodies
685 used were Li-COR goat anti-rat IRDye 800 (1:15,000), goat anti-rabbit IRDye 680 (1:15,000) and
686 goat anti-mouse IRDye 680 (1:15,000). Band densities were quantified using Image Studio
687 (Odyssey Infrared Imaging System (LI-COR, Lincoln, Nebraska).
688 ***Drosophila* Rearing and Stocks:** All *Drosophila melanogaster* strains were grown and
689 maintained on standard cornmeal-molasses media at 25 °C under a 12:12 h light-dark schedule.
690 Fly stocks include w^{1118} ((Bloomington Indiana Stock Center (BI) 6326), TH-GAL4 (BI 8848),
691 $DAT^{MB07315}$ (BI 25547), UAS-mCherry (Kyoto Stock Center 109594), and M[vas-int.Dm]ZH-2A;
692 (M[3xP3-RFP.attP']ZH-22A (BI 24481) and DAT^{fmn} (dDAT KO). *Drosophila* expressing
693 homozygous dDAT null allele DAT^{fmn} (dDAT KO) (Kume et al., 2005), TH-Gal4 (Friggi-Grelin et
694 al., 2003), and UAS-mCherry were outcrossed to a control line (w^{1118}) for 5 - 10 generations and
695 selected by PCR or eye color. Transgenes (hDAT WT and hDAT RT445C) were cloned into pBID-
696 UASC (Wang et al., 2012) and constructs were injected into embryos from M[vas-int.Dm]ZH-2A,
697 M[3xP3-RFP.attP']ZH-22A (BI 24481) (Rainbow Transgenic Flies Inc; Camarillo, CA). Initial
698 potential transformants were isolated and selected. Flies containing transgenes were outcrossed
699 to dDAT KO flies (in w^{1118} background) for 5–10 generations. Age-paired adult male flies (10 days

post eclosion) containing a single copy of hDAT WT or hDAT R445C in DA neurons in a *DAT^{fmn}* background were used for all subsequent experiments.

***Drosophila* amperometry assays:** *Drosophila* brains were dissected with surgical forceps in ice-cold Schneider's *Drosophila* Medium supplemented with 1.5% BSA. Whole brains were placed in a mesh holder in Lub's external solution (see previous). A carbon fiber electrode was held at +600 mV and inserted juxtaposed to TH-positive PPL1 DA neuronal region. After establishing a baseline, 20 μM AMPH was added to the bath. Amperometric currents were processed as stated above.

***Drosophila* locomotion analysis:** Spontaneous locomotor activity in an open field was measured using custom 3D printed activity chambers (1.1 x 1.1 cm). Locomotion was detected using NIS Elements AR (Melville, NY). Animals were placed in the activity chambers, where activity was recorded for 5 min following 2-min acclimation period. Data from this test was also used to measure anxiety-like behaviors. Thigmotaxis, the tendency of an animal to remain close to the walls of an open field, was measured as the percent of time flies spent in center square (3.0 x 3.0 mm). Total distance traveled, center time, and velocity distribution were quantified using MATLAB 2018b (MathWorks; Natick, MA). Velocity thresholds for movement initiation were set based on the average velocity during non-movement phases ($\chi + 0.5\sigma$ = 0.50 + 0. 24 mm/s), whereas fast movement was determined from the average velocity during the test period ($\chi + \sigma$ = 2.7 + 2.6 mm/s).

***Drosophila* grooming analysis:** Flies were observed for a period of 5 min (~19 fps). Forelimb and hindlimb grooming incidents were quantified per frame, where total grooming time was calculated as the total number of frames spent grooming.

***Drosophila* flight assay**: Coordinated flight was measured using custom 3D-printed chambers (3.9 x 1.0 x 1.0 cm) filled with 2600 μL of water. Flight initiation was recorded at 2,000 frames per second using a Phantom v1212 Camera (Ametek; Wayne, New Jersey), after a short acclimation

period. Delay in flight initiation was quantified as the time from the outset of the first wing motion to the coordinated jump response.

HPLC: Biogenic amines were quantified by the Neurochemistry Core Facility at Vanderbilt University. Briefly, *Drosophila* brains were dissected quickly in ice-cold PBS and immediately frozen in liquid nitrogen. Brains were homogenized using a tissue dismembrator in 100 – 750 μl of solvent containing (in mM) 100 TCA, 10 Na, 0.1 EDTA and 10.5% methanol (pH 3.8). Homogenate was spun (10,000 x g, 20 min) and supernatant was removed for biogenic monoamines analysis. Biogenic amine concentrations were determined utilizing an Antec Decade II (oxidation: 0.65) electrochemical detector operated at 33 °C. Supernatant was injected using a Water 2707 autosampler onto a Phenomenex Kintex C18 HPLC column (100 x 4.60 mm, 2.6 μm). Biogenic amines were eluted with a mobile phase 89.5% of solvent (see previous) and 10.5 % methanol (pH 3.8). Solvent was delivered at 0.6 ml/min using a Waters 515 HPLC pump. Biogenic amines elute in the following order: Noradrenaline, Adrenaline, DOPAC, Dopamine, 5-HIAA, HVA, 5-HT, and 3-MT. HPLC control and data acquisition are managed by Empower software. Isoproterenol (5 ng/mL) was included in the homogenization buffer for use as a standard to quantify the biogenic amines. Protein concentration was determined by BCA Protein Assay Kit (ThermoFisher Scientific).

Immunohistochemistry: Fly brains were dissected in PBS and fixed in 4% paraformaldehyde for 20 mins at RT. Brains were washed 3 times with PBST (0.3% Triton X100). Brains were blocked in 1% BSA and 5% normal goat serum. Brains were immunostained for TH (1:200; Millipore, AB152) and nc82 (1:50; DSHB) overnight at 4 °C, washed and stained with secondary antibodies Alexa 488–conjugated goat anti-rabbit (1:200; A11034, ThermoFisher Scientific) and Alexa 566–conjugated goat anti-mouse (1:200, A11031, ThermoFisher Scientific) overnight at 4 °C. Brains were washed and mounted with ProLong Diamond Anti-Fade mounting solution (ThermoFisher Scientific). Imaging was performed using a Nikon A1R

confocal microscope. The resolution of the image stack was 1024 × 1024 with 0.5 µm step size. Neurons were counted manually using FIJI (Bethesda, MD).

Rosetta Homology Modeling and Stability Calculations: The Rosetta Flex ΔΔG protocol (Barlow et al., 2018; Kuenze et al., 2019) and the Rosetta Membrane all-atom energy function (Alford et al., 2015) were used to estimate free energy changes and sample conformational changes of the LeuT, hDAT and corresponding variants. The Flex ΔΔG protocol models mutation-induced conformational and energetic changes through a series of "backrub" moves of the protein backbone together with side-chain repacking around the mutation site. 15,000 backrub steps were used in this study to sample backbone and side chain degrees of freedom for neighboring residues within an 9 Å boundary of the mutation site. This is subsequently followed by side chain optimization using the Rosetta "packer." Global minimization of the backbone and side chains torsion angles is performed with harmonic Cα atom-pair distance restraints. The restraints are used to prevent large structural deviations from the input model. Models are scored with the Rosetta Membrane all-atom energy function (Alford et al., 2015). This is carried out in parallel for the WT input model and the mutant of interest. For the LeuT calculations, the LeuT crystal structure (PDB ID: 2A65) (Yamashita et al., 2005) was used and 1000 independent trajectories were carried out for both LeuT WT (control) and each variant. For the hDAT calculations, homology models for hDAT WT were created in the Rosetta molecular modeling suite (revision 57712, Rosetta Commons) as previously described (Campbell et al., 2019) using the *Drosophila melanogaster* DAT (PDB ID: 4XP9) (Wang et al., 2015) as a structural template. 500 independent trajectories were carried out for each hDAT R445 mutant and hDAT WT (control). This protocol was used for the top three scoring hDAT homology models resulting in 1500 trajectories total per mutant. The Rosetta energy change (ΔΔG) was calculated as score difference between the average of the top 5% of LeuT WT and corresponding variants, as well as of hDAT WT and corresponding variants. Rosetta ΔΔG values are in Rosetta Energy Units (REU). Representative structural models for LeuT, hDAT, and all variants were selected for visualization in Pymol by

776 removing outliers and taking the lowest-energy model within the lowest interquartile range of a
777 box plot.

778 **Protein expression and purification:** Escherichia coli C41 (DE3) cells were transformed with
779 the pET16b plasmid containing LeuT, LeuT R375A, LeuT R375C or LeuT R375D tagged with a
780 C-Terminal 8xHis-tag and thrombin cleavage site. Transformed cells were grown in Terrific broth
781 media to an OD_{600} of 0.6. Cells were induced with 0.1 mM isopropyl-β-D-1-thiogalactopyranoside
782 (20 h, 20 °C), harvested by centrifugation and disrupted with a french press in 20 mM HEPES-
783 Tris pH 7.5, 190 mM NaCl, 10 mM KCl, 1 mM EDTA, 5 mM L-Alanine, 100 μM AEBSF and 0.004
784 mg/mL DNAse I. Cells membranes were isolated by ultracentrifugation at 200,000 x g (45 min)
785 and solubilised with 40 mM n-dodecyl-β-D-maltopyranoside (DDM, Anatrace). Solubilised
786 membranes were incubated with Ni-NTA resin (Qiagen) (1 h, 4 °C). Protein bound to the Ni-NTA
787 resin was washed with 50 mM imidiazole and then eluted with 300 mM imidiazole. The histidine
788 tag was subsequently removed by digestion with thrombin (10 U/mg protein) and the protein
789 further purified on a size exclusion column in 10 mM Tris-HCl pH 8.0, 45 mM NaCl, 5 mM KCl, 5
790 mM L-Alanine and 40 mM n-Octyl-β-D-glucopyranoside (OG, Anatrace). Purified protein was
791 concentrated to 8 mg/mL using 30 kDa cut-off AMICON concentrators (Merck).

792 **Crystallography and structure determination:** Crystals were grown at 18 °C using the hanging-
793 drop vapor diffusion method, by mixing protein (~8 mg/ml) and well solution (1:1 vol:vol), 100 mM
794 HEPES-NaOH pH 7-7.5, 200 mM NaCl, 17-22% PEG550 MME. Protein crystals were
795 cryoprotected by soaking in the well solution supplemented with 25 – 35% PEG550 MME. All
796 diffraction data was collected on the EIGER 16M detector at the Australian Synchrotron (ACRF
797 ANSTO) beamline MX2 at a wavelength of 0.954 Å (Aragao et al., 2018). Datasets were indexed,
798 integrated and scaled using XDS (Kabsch, 2010). Initial phases were obtained by molecular
799 replacement with Phaser (McCoy et al., 2007) using the structure of LeuT with bound L-Leu (PDB
800 ID: 3F3E) as the search model. The protein model was built manually in Coot (Emsley et al., 2010)

and refined using REFMAC (Murshudov et al., 2011) with TLS and non-crystallographic symmetry (NCS) restraints (Winn et al., 2001). Phases were further improved by rounds of manual rebuilding followed by restrained refinement in REFMAC. Validation was carried out using MolProbity (Chen et al., 2010). Unit cell parameters, data collection and refinement statistics are presented in Table1. All structural figures were prepared using USCF Chimera (Pettersen et al., 2004).

Electron Paramagnetic Resonance (EPR) protocol: Cysteine residues were introduced using site directed mutagenesis into LeuT, LeuT R375A, and LeuT R375D constructs. Experiments were conducted as in Claxton *et al.* (Claxton et al., 2010). The apo conformation refers to Na^+ and leucine-free transporter, while the +Na/Leu state was obtained in 200 mM NaCl and 4-fold molar excess of Leu relative to LeuT. Double Electron Electron Resonance (DEER) (Jeschke and Polyhach, 2007) was performed at 83K on a Bruker 580 pulsed EPR spectrometer operating at Q-band frequency using a standard 4-pulse sequence (Zou and McHaourab, 2010). DEER echo decays were analyzed to obtain distance distributions (Jeschke et al., 2002).

Statistical methods: Experiments were designed using statistical power calculations considering means and standard errors from preliminary data. Statistical analyses were performed using GraphPad Prism 8 (San Diego, CA). Shapiro-Wilk normality tests were performed to determine if data was normally distributed and F tests were performed to compare variances; parametric or non-parametric tests with appropriate corrections were chosen accordingly. All data was acquired unblinded, but analyzed blinded to genotype.

Molecular dynamics (MD) simulations: The structural model for *apo* hDAT (residues Q58-D600) in the outward-facing open (OF) unbound state, based on dDAT structure (PDB ID: 4M48), was taken from previous study (Cheng et al., 2018). Four simulation systems using this initial structure were constructed: wild-type (WT), R445C, R445A, and R445D. In each case, the transporter is embedded into 1-palmitoyl-2-oleoyl-sn-glycero-3-phosphocholine (POPC) membrane lipids using CHARMM-GUI Membrane Builder module (Wu et al., 2014). TIP3P waters and Na^+ and Cl^- ions corresponding to 0.15 M NaCl solution were added to build a simulation box

of ~110 ×110 ×118 Å (Phillips et al., 2005). Each simulation system contained ~ 131,000 atoms, the transporter, ~ 300 lipid molecules, and 27,000 water molecules. All simulations were performed using NAMD (Phillips et al., 2005) (version NAMD_2.12) following previous protocol (Cheng et al., 2018). For each mutant, two independent runs of 200 ns are performed to verify the reproducibility of the results. VMD (Humphrey et al., 1996) with in-house scripts was used for visualization and trajectory analysis.

AUTHOR CONTRIBUTIONS

JIA and AG conceptualized the study. JIA, JF, MHC, ACS, KL, AD, LS, ANB, YZ, and SJM carried out the experiments. JIA, MHC, JF, ACS, HSM, AMC and KL conducted formal analyses of the data, prepared the figures and contributed to writing the manuscript. CFF, AMC and MAK provided guidance, expertise and interpretations of results on select topics. AG, HJGM, JM, RMR, HSM, and IB acquired funding, supervised the study and interpreted results. All authors contributed to the editing and review of the manuscript.

ACKNOWLEDGEMENTS

The authors would like to acknowledge Saunders Consulting for the help in editing this manuscript. This research was undertaken in part using the MX2 beamline at the Australian Synchrotron, part of ANSTO, and made use of the Australian Cancer Research Foundation (ACRF) detector. Research reported in this publication was supported by NIH R01-DA038058 (AG), NIH R01-DA035263 (AG, HJGM), NIH F31-MH114316 (JIA), NIH P41-GM103712 (IB) and NIH P30-DA035778 (IB), and by the Intramural Research Program of the NIH, NIDA Z1A DA000606 (LS). The content is solely the responsibility of the authors and does not necessarily represent the official views of the National Institutes of Health.

CONFLICTS OF INTEREST

853 The authors have declared no conflicts of interest.

854

855 **FIGURE LEGENDS**

856 **Figure 1: R445C variant disrupts locomotive behaviors in *Drosophila***

857 (**A**) hDAT WT or hDAT R445C was selectively expressed in DA neurons in a dDAT KO (*fmn*)
858 background. Representative trajectories of hDAT WT (*black*) and hDAT R445C (*blue*) flies in an
859 open-field test during a 5-min test period. 3 x 3 mm square (*red dashed lines*) delineates the
860 center space. (**B**) hDAT WT and hDAT R445C flies spent comparable time in the center space ($p > 0.05$; $n = 35$). (**C**) hDAT R445C flies traveled significantly less relative to hDAT WT flies ($p = 0.006$; $n = 35$). (**D**) Histogram represents instantaneous velocities ranging from 0.74 to 10.0 mm/s
863 (bin width = 0.094 mm/s; see methods) and corresponding frequencies (number of times) for
864 hDAT WT (*gray bars*) and hDAT R445C (*blue bars*) flies. Initiating movement velocities (0.74 -
865 0.94 mm/s, *orange shaded*), fast movement velocities (5.3 - 10.0 mm/s, *green shaded*), average
866 velocity ($\bar{x}$) are highlighted. (**E**) hDAT R445C flies spent a comparable amount of time initiating
867 movement relative to hDAT WT flies ($p > 0.05$; $n = 35$). (**F**) hDAT WT flies spent significantly more
868 time in fast movement compared with hDAT R445C flies ($p = 0.001$; $n = 35$). Data represent mean
869 ± SEM. Welch's t-test: (B); Mann-Whitney test (C) and (E - F).

870 **Figure 2. R445C variant selectively impairs coordinated motor behaviors, such as take-off,**
871 **but not repetitive motor behaviors, such as grooming**

872 (**A**) Representative single frames of *Drosophila* hDAT WT (*top*) and hDAT R445C (*bottom*) during
873 various phases of coordinated take-off (video recorded at 2000 fps). (**B**) Flight initiation (take-off)
874 was quantified from the initial phase of wing elevation (t = 0) to the second phase of simultaneous
875 wing depression and leg extension. Flight initiation was significantly delayed in hDAT R445C flies
876 relative to hDAT WT ($p = 0.03$; $n = 10 - 11$). (**C**) hDAT R445C flies spent comparable time

877 grooming compared with hDAT WT flies ($p > 0.05$; $n = 35$). Data represent mean ± SEM. Welch's
878 t-test: (B); Mann-Whitney test (C).

879 **Figure 3. Reduced brain DA content and AMPH-induced DA efflux in hDAT R445C flies**

880 (**A**) Tissue concentration of DA (*left*) and 5-HT (*right*) measured by HPLC ($n = 4$, 20 brains per
881 measurement). DA content was significantly decreased in hDAT R445C relative to hDAT WT
882 brains ($p = 0.01$). 5-HT content in hDAT R445C was comparable to hDAT WT ($p > 0.05$). (**B**)
883 Confocal z-stack (5 µm) of hDAT WT (*left*) and hDAT R445C (*center*) brains co-stained with anti-
884 TH (*magenta*) and anti-n82 (*cyan*) zoomed-in on PPL1 neurons. Quantitation of TH-positive PPL1
885 neurons showed a significant reduction of these neurons in hDAT R445C brains relative to hDAT
886 WT ($p < 0.0001$; $n = 8 – 11$; *right*) (**C**) Diagram illustrates amperometric studies in *Drosophila*
887 brains in which a carbon fiber electrode records currents from TH-positive PPL1 DA neuronal
888 region (*red box*) in response to AMPH application (20 µM; *left).* AMPH-induced (arrow)
889 amperometric currents in hDAT WT (*black trace*) and hDAT R445C (*blue trace*) brains.
890 Quantitation of peak currents showed a significant decrease in DA efflux measured in hDAT
891 R445C relative to hDAT WT ($p = 0.04$; $n = 7$; *right*). Data represent mean ± SEM. Student's t-test
892 (A)-(B); Welch's t-test: (C).

893 **Figure 4. Representative Rosetta models and crystallographic structures of LeuT revealed**
894 **weakening of E6-R375 salt bridge promoted by substitutions at R375 (corresponding to**
895 **R445 in hDAT)**

896 (**A**) Models derived, using Rosetta, of LeuT WT (*left*), LeuT R375A (*middle*) and LeuT R375D
897 (*right*) where protein backbones are represented as cartoons and residues E6, I184, I187, R5,
898 and D369 are represented as green spheres and sticks. K189 is colored in blue throughout each
899 model. R375 is colored in green (*left*). A375 is colored in cyan (*middle*). D375 is colored in yellow
900 (*right)*. All corresponding polar contacts between side chain or backbone atoms in each model
901 are represented as dashed lines in black. R375 substitution to either Ala or Asp disrupted E6-

902 R375 salt bridge. (**B**) Crystal structures of LeuT WT (*green*), LeuT R375A (*cream*) and LeuT
903 R375D (grey) are superimposed. Box indicates area of zoomed-in view of TM1-TM8 IC region for
904 LeuT WT (top *left*), LeuT R375D (top *right*), LeuT R375A (bottom left) and overlay of three
905 structures (*bottom right*). Distances between residues are shown in dashed lines.

906 **Figure 5. Asp substitution at R375 in LeuT favors an inward facing conformation**

907 Probability distance distributions (P(r)) of the spin labels 308/409 and 7/86 (**A**) reporting the
908 conformational dynamics of the EC (*left*) and IC (*right*) gate of LeuT, respectively. Distance
909 distributions for each pair were obtained in the Apo (*black*), Na^+-bound (Na^+; *red*), and Na^+- and
910 Leu-bound (Na^+/ Leu; *blue*) conformations for LeuT WT (**B**), LeuT R375A (**C**) and LeuT R375D
911 (**D**).

912 **Figure 6. hDAT R445C favors the opening of the IC vestibule, leading to intermittent**
913 **formation of a channel-like intermediate.**

914 (**A**) Structure of hDAT WT in the OF state (*white*) illustrates a network of interactions at the IC
915 surface stabilizing the closure of IC vestibule and solvated EC vestibule (*gray shaded region).* (**B**)
916 Substitution of R445 with Cys (*orange*) breaks salt-bridge R445-E428, which weakens IC network
917 interactions and promotes the intermittent formation of a channel-like intermediate. This
918 conformation favors the entry of both water and ions from the IC space. Hydrated regions inside
919 the transporter are indicated in *gray* shaded areas with explicit water molecules displayed in
920 spheres and lines (CPK format). Green and purple spheres are Na^+ migrating from the EC and
921 IC side, respectively. (**C**) Structural alignment of hDAT R445C (*orange*) with hDAT WT (*white*). In
922 hDAT R445C, the association between TM8 and TM9 (near the IC exposed region) is weakened.
923 TM9 undergoes an outward titling (*blue curved arrow*) to allow for the 'opening' of IC vestibule
924 along TM8, facilitated by the absence of C445-E428 salt bridge (R445-E428 in hDAT WT holds
925 TM8-TM9 in place). (**D-F**) Results from MD simulations of hDAT R445C. Time evolution of
926 distances between Na^+ and D79 (**D**); between salt-bridge forming residues at EC and IC regions
927 (**E**) are displayed. On the EC side, D476-R85 distance decreases (EC gate closure). On the IC

side, D436-R60 distance increases (IC gate opening). D345-K66 remains closed. After dissociating from D436 (t = 150 ns), R60 interacts with E428 (t = 200 ns). (**F**) Interhelical distances for EC-exposed TM1b-TM10 and TM6a-TM10 shows that the EC region remains exposed to solvent with reduced opening, and IC-exposed TM1a-TM6b is closed, but there is a new opening indicated by the increase in TM6b-TM9 distance. Conformation shown in B is the last snapshot taken from the simulation trajectory in **D-F**.

Figure 7. CQ enhances R445C expression ratios and flight coordination

(**A**) Representative immunoblots of surface hDAT (top *left*), total hDAT (top *right*) and corresponding Na-K ATPase (*bottom left)* and actin (*bottom right)* loading controls. hDAT expression was normalized to hDAT WT. hDAT R445C displayed significantly reduced surface ($p < 0.0001$; n = 4, in triplicate) and total glycosylated (#) expression relative to hDAT WT ($p < 0.0001$; n = 4, in triplicate). (**B**) Average ^{3}[H]DA saturation curves of DA uptake measured in hDAT WT (*black*) or hDAT R445C (*blue*) cells (n = 3, in triplicate). Curves were fit to Michaelis-Menten kinetics to derive K_m and V_{max}. DA uptake for hDAT R445C was significantly reduced compared with hDAT WT at every DA concentration measured ($F_{(6,64)} = 52.4$, $p < 0.0001$), as were the kinetic constants, K_m and V_{max} ($p < 0.0001$). (**C**) Representative traces of amperometric currents (DA efflux) recorded in response to AMPH application (*left*; 10 μM, indicated by arrow) from hDAT WT (*black*) and hDAT R445C (*blue*) cells loaded with DA (2 mM, 10 min) with whole-cell pipette. Quantitation of peak current amplitudes illustrated a significant reduction in DA efflux recorded from hDAT R445C compare to hDAT WT (*right*; p = 0.008; n = 6-7). (**D**) Representative immunoblots of total hDAT (*top*) and actin loading controls (*bottom),* where glycosylated (#) and non-glycosylated (*) hDAT is highlighted. Ratio of mature (glycosylated) to immature (non-glycosylated) DAT (mDAT/iDAT) expression following CQ treatment was normalized to vehicle condition for hDAT WT and hDAT R445C cells (n = 4, in duplicate). Incubating hDAT R445C cells with CQ (1 mM, 4 h) significantly increased the ratio of mDAT/iDAT ($F_{(1,20)} = 18.0$), p = 0.003). CQ also significantly increased mDAT/iDAT expression in hDAT WT cells (p = 0.04). (**E**) Diagramed

954 is the flight initiation assay used to determine take-off times for hDAT WT and hDAT R445C
955 *Drosophila* (*left*). hDAT R445C and hDAT WT *Drosophila* were fed CQ (3 mM, 72 h) or vehicle
956 supplemented diet. Quantitation showed a significant reduction in the time to initiate flight in hDAT
957 R445C flies ($F_{(1,29)}$ = 8.7 , p = 0.04) in response to CQ compared with vehicle conditions (*right*).
958 Time for flight initiation was comparable in hDAT WT flies exposed to CQ and vehicle
959 supplemented diet (p > 0.05). Data represent mean ± SEM. Student's t-test (A) and (C); Two-way
960 ANOVA with Bonferroni's multiple comparison test: (B), and (D-E).
961
962 **REFERENCES**

963 Achan, J., Talisuna, A.O., Erhart, A., Yeka, A., Tibenderana, J.K., Baliraine, F.N., Rosenthal, P.J.,
964 and D'Alessandro, U. (2011). Quinine, an old anti-malarial drug in a modern world: role in the
965 treatment of malaria. Malar J *10*, 144.
966 Alford, R.F., Koehler Leman, J., Weitzner, B.D., Duran, A.M., Tilley, D.C., Elazar, A., and Gray,
967 J.J. (2015). An Integrated Framework Advancing Membrane Protein Modeling and Design. PLoS
968 computational biology *11*, e1004398.
969 Anderson, D.J., and Adolphs, R. (2014). A framework for studying emotions across species. Cell
970 *157*, 187-200.
971 Aragao, D., Aishima, J., Cherukuvada, H., Clarken, R., Clift, M., Cowieson, N.P., Ericsson, D.J.,
972 Gee, C.L., Macedo, S., Mudie, N.*, et al.* (2018). MX2: a high-flux undulator microfocus beamline
973 serving both the chemical and macromolecular crystallography communities at the Australian
974 Synchrotron. J Synchrotron Radiat *25*, 885-891.
975 Asjad, H.M.M., Kasture, A., El-Kasaby, A., Sackel, M., Hummel, T., Freissmuth, M., and Sucic, S.
976 (2017). Pharmacochaperoning in a Drosophila model system rescues human dopamine
977 transporter variants associated with infantile/juvenile parkinsonism. The Journal of biological
978 chemistry *292*, 19250-19265.

Aso, Y., Herb, A., Ogueta, M., Siwanowicz, I., Templier, T., Friedrich, A.B., Ito, K., Scholz, H., and Tanimoto, H. (2012). Three dopamine pathways induce aversive odor memories with different stability. PLoS genetics *8*, e1002768.

Barlow, K.A., Ó Conchúir, S., Thompson, S., Suresh, P., Lucas, J.E., Heinonen, M., and Kortemme, T. (2018). Flex ddG: Rosetta Ensemble-Based Estimation of Changes in Protein–Protein Binding Affinity upon Mutation. J Phys Chem B *122*, 5389-5399.

Barone, M.C., Sykiotis, G.P., and Bohmann, D. (2011). Genetic activation of Nrf2 signaling is sufficient to ameliorate neurodegenerative phenotypes in a Drosophila model of Parkinson's disease. Dis Model Mech *4*, 701-707.

Beerepoot, P., Lam, V.M., and Salahpour, A. (2016). Pharmacological Chaperones of the Dopamine Transporter Rescue Dopamine Transporter Deficiency Syndrome Mutations in Heterologous Cells. The Journal of biological chemistry *291*, 22053-22062.

Belovich, A.N., Aguilar, J.I., Mabry, S.J., Cheng, M.H., Zanella, D., Hamilton, P.J., Stanislowski, D.J., Shekar, A., Foster, J.D., Bahar, I.*, et al.* (2019). A network of phosphatidylinositol (4,5)-bisphosphate (PIP2) binding sites on the dopamine transporter regulates amphetamine behavior in Drosophila Melanogaster. Molecular psychiatry.

Berry, J.A., Cervantes-Sandoval, I., Nicholas, E.P., and Davis, R.L. (2012). Dopamine is required for learning and forgetting in Drosophila. Neuron *74*, 530-542.

Beuming, T., Shi, L., Javitch, J.A., and Weinstein, H. (2006). A comprehensive structure-based alignment of prokaryotic and eukaryotic neurotransmitter/Na+ symporters (NSS) aids in the use of the LeuT structure to probe NSS structure and function. Molecular pharmacology *70*, 1630-1642.

Bischof, J., Maeda, R.K., Hediger, M., Karch, F., and Basler, K. (2007). An optimized transgenesis system for Drosophila using germ-line-specific phiC31 integrases. Proc Natl Acad Sci U S A *104*, 3312-3317.

1004 Bjorklund, A., and Dunnett, S.B. (2007). Fifty years of dopamine research. Trends in
1005 neurosciences *30*, 185-187.
1006 Borre, L., Andreassen, T.F., Shi, L., Weinstein, H., and Gether, U. (2014). The second sodium
1007 site in the dopamine transporter controls cation permeation and is regulated by chloride. The
1008 Journal of biological chemistry *289*, 25764-25773.
1009 Bowton, E., Saunders, C., Erreger, K., Sakrikar, D., Matthies, H.J., Sen, N., Jessen, T., Colbran,
1010 R.J., Caron, M.G., Javitch, J.A.*, et al.* (2010). Dysregulation of dopamine transporters via
1011 dopamine D2 autoreceptors triggers anomalous dopamine efflux associated with attention-deficit
1012 hyperactivity disorder. J Neurosci *30*, 6048-6057.
1013 Bowton, E., Saunders, C., Reddy, I.A., Campbell, N.G., Hamilton, P.J., Henry, L.K., Coon, H.,
1014 Sakrikar, D., Veenstra-VanderWeele, J.M., Blakely, R.D.*, et al.* (2014). SLC6A3 coding variant
1015 Ala559Val found in two autism probands alters dopamine transporter function and trafficking.
1016 Translational psychiatry *4*, e464.
1017 Brand, A.H., and Perrimon, N. (1993). Targeted gene expression as a means of altering cell fates
1018 and generating dominant phenotypes. Development *118*, 401-415.
1019 Cackovic, J., Gutierrez-Luke, S., Call, G.B., Juba, A., O'Brien, S., Jun, C.H., and Buhlman, L.M.
1020 (2018). Vulnerable Parkin Loss-of-Function Drosophila Dopaminergic Neurons Have Advanced
1021 Mitochondrial Aging, Mitochondrial Network Loss and Transiently Reduced Autophagosome
1022 Recruitment. Front Cell Neurosci *12*, 39.
1023 Campbell, N.G., Shekar, A., Aguilar, J.I., Peng, D., Navratna, V., Yang, D., Morley, A.N., Duran,
1024 A.M., Galli, G., O'Grady, B.*, et al.* (2019). Structural, functional, and behavioral insights of
1025 dopamine dysfunction revealed by a deletion in SLC6A3. Proc Natl Acad Sci U S A *116*, 3853-
1026 3862.
1027 Card, G., and Dickinson, M. (2008). Performance trade-offs in the flight initiation of Drosophila.
1028 The Journal of experimental biology *211*, 341-353.

1029 Cartier, E., Garcia-Olivares, J., Janezic, E., Viana, J., Moore, M., Lin, M.L., Caplan, J.L., Torres,
1030 G., and Kim, Y.H. (2019). The SUMO-Conjugase Ubc9 Prevents the Degradation of the
1031 Dopamine Transporter, Enhancing Its Cell Surface Level and Dopamine Uptake. Front Cell
1032 Neurosci *13*, 35.
1033 Cartier, E., Hamilton, P.J., Belovich, A.N., Shekar, A., Campbell, N.G., Saunders, C., Andreassen,
1034 T.F., Gether, U., Veenstra-Vanderweele, J., Sutcliffe, J.S.*, et al.* (2015). Rare autism-associated
1035 variants implicate syntaxin 1 (STX1 R26Q) phosphorylation and the dopamine transporter (hDAT
1036 R51W) in dopamine neurotransmission and behaviors. EBioMedicine *2*, 135-146.
1037 Chai, C., and Lim, K.L. (2013). Genetic insights into sporadic Parkinson's disease pathogenesis.
1038 Curr Genomics *14*, 486-501.
1039 Chen, V.B., Arendall, W.B., 3rd, Headd, J.J., Keedy, D.A., Immormino, R.M., Kapral, G.J., Murray,
1040 L.W., Richardson, J.S., and Richardson, D.C. (2010). MolProbity: all-atom structure validation for
1041 macromolecular crystallography. Acta Crystallogr D Biol Crystallogr *66*, 12-21.
1042 Cheng, M.H., and Bahar, I. (2014). Complete mapping of substrate translocation highlights the
1043 role of LeuT N-terminal segment in regulating transport cycle. PLoS computational biology *10*,
1044 e1003879.
1045 Cheng, M.H., and Bahar, I. (2015). Molecular mechanism of dopamine transport by human
1046 dopamine transporter. Structure *23*, 2171-2181.
1047 Cheng, M.H., and Bahar, I. (2019). Monoamine transporters: structure, intrinsic dynamics and
1048 allosteric regulation. Nat Struct Mol Biol *26*, 545-556.
1049 Cheng, M.H., Kaya, C., and Bahar, I. (2018). Quantitative Assessment of the Energetics of
1050 Dopamine Translocation by Human Dopamine Transporter. J Phys Chem B *122*, 5336-5346.
1051 Claridge-Chang, A., Roorda, R.D., Vrontou, E., Sjulson, L., Li, H., Hirsh, J., and Miesenbock, G.
1052 (2009). Writing memories with light-addressable reinforcement circuitry. Cell *139*, 405-415.

1053 Claxton, D.P., Quick, M., Shi, L., de Carvalho, F.D., Weinstein, H., Javitch, J.A., and McHaourab,
1054 H.S. (2010). Ion/substrate-dependent conformational dynamics of a bacterial homolog of
1055 neurotransmitter:sodium symporters. Nat Struct Mol Biol *17*, 822.
1056 Coleman, J.A., Yang, D., Zhao, Z., Wen, P.-C., Yoshioka, C., Tajkhorshid, E., and Gouaux, E.
1057 (2019). Serotonin transporter–ibogaine complexes illuminate mechanisms of inhibition and
1058 transport. Nature *569*, 141.
1059 Daniels, G.M., and Amara, S.G. (1999). Regulated trafficking of the human dopamine transporter.
1060 Clathrin-mediated internalization and lysosomal degradation in response to phorbol esters. The
1061 Journal of biological chemistry *274*, 35794-35801.
1062 DiCarlo, G.E., Aguilar, J.I., Matthies, H.J., Harrison, F.E., Bundschuh, K.E., West, A., Hashemi,
1063 P., Herborg, F., Rickhag, M., Chen, H.*, et al.* (2019). Autism-linked dopamine transporter mutation
1064 alters striatal dopamine neurotransmission and dopamine-dependent behaviors. J Clin Invest
1065 *129*, 3407-3419.
1066 Emsley, P., Lohkamp, B., Scott, W.G., and Cowtan, K. (2010). Features and development of Coot.
1067 Acta Crystallogr D Biol Crystallogr *66*, 486-501.
1068 Faivre, F., Joshi, A., Bezard, E., and Barrot, M. (2019). The hidden side of Parkinson's disease:
1069 Studying pain, anxiety and depression in animal models. Neuroscience and biobehavioral reviews
1070 *96*, 335-352.
1071 Feany, M.B., and Bender, W.W. (2000). A Drosophila model of Parkinson's disease. Nature *404*,
1072 394-398.
1073 Ford, C.P. (2014). The role of D2-autoreceptors in regulating dopamine neuron activity and
1074 transmission. Neuroscience *282*, 13-22.
1075 Forrest, L.R., Zhang, Y.W., Jacobs, M.T., Gesmonde, J., Xie, L., Honig, B.H., and Rudnick, G.
1076 (2008). Mechanism for alternating access in neurotransmitter transporters. Proc Natl Acad Sci U
1077 S A *105*, 10338-10343.

1078 Friggi-Grelin, F., Coulom, H., Meller, M., Gomez, D., Hirsh, J., and Birman, S. (2003). Targeted
1079 gene expression in Drosophila dopaminergic cells using regulatory sequences from tyrosine
1080 hydroxylase. J Neurobiol *54*, 618-627.
1081 Giovannoni, G., O'Sullivan, J.D., Turner, K., Manson, A.J., and Lees, A.J. (2000). Hedonistic
1082 homeostatic dysregulation in patients with Parkinson's disease on dopamine replacement
1083 therapies. J Neurol Neurosurg Psychiatry *68*, 423-428.
1084 Giros, B., and Caron, M.G. (1993). Molecular characterization of the dopamine transporter.
1085 Trends in pharmacological sciences *14*, 43-49.
1086 Hamilton, P.J., Belovich, A.N., Khelashvili, G., Saunders, C., Erreger, K., Javitch, J.A., Sitte, H.H.,
1087 Weinstein, H., Matthies, H.J.G., and Galli, A. (2014). PIP2 regulates psychostimulant behaviors
1088 through its interaction with a membrane protein. Nat Chem Biol *10*, 582-589.
1089 Hamilton, P.J., Campbell, N.G., Sharma, S., Erreger, K., Herborg Hansen, F., Saunders, C.,
1090 Belovich, A.N., Consortium, N.A.A.S., Sahai, M.A., Cook, E.H.*, et al.* (2013). De novo mutation in
1091 the dopamine transporter gene associates dopamine dysfunction with autism spectrum disorder.
1092 Molecular psychiatry *18*, 1315-1323.
1093 Hansen, F.H., Skjorringe, T., Yasmeen, S., Arends, N.V., Sahai, M.A., Erreger, K., Andreassen,
1094 T.F., Holy, M., Hamilton, P.J., Neergheen, V.*, et al.* (2014). Missense dopamine transporter
1095 mutations associate with adult parkinsonism and ADHD. J Clin Invest *124*, 3107-3120.
1096 Hartenstein, V., and Stollewerk, A. (2015). The evolution of early neurogenesis. Dev Cell *32*, 390-
1097 407.
1098 Hastrup, H., Sen, N., and Javitch, J.A. (2003). The human dopamine transporter forms a tetramer
1099 in the plasma membrane: cross-linking of a cysteine in the fourth transmembrane segment is
1100 sensitive to cocaine analogs. The Journal of biological chemistry *278*, 45045-45048.
1101 Humphrey, W., Dalke, A., and Schulten, K. (1996). VMD: visual molecular dynamics. Journal of
1102 molecular graphics *14*, 33-38, 27-38.

1103 Ingram, S.L., Prasad, B.M., and Amara, S.G. (2002). Dopamine transporter-mediated
1104 conductances increase excitability of midbrain dopamine neurons. Nat Neurosci *5*, 971-978.
1105 Jenner, P. (2015). Treatment of the later stages of Parkinson's disease - pharmacological
1106 approaches now and in the future. Transl Neurodegener *4*, 3.
1107 Jeschke, G., Koch, A., Jonas, U., and Godt, A. (2002). Direct conversion of EPR dipolar time
1108 evolution data to distance distributions. Journal of magnetic resonance *155*, 72-82.
1109 Jeschke, G., and Polyhach, Y. (2007). Distance measurements on spin-labelled
1110 biomacromolecules by pulsed electron paramagnetic resonance. Physical chemistry chemical
1111 physics : PCCP *9*, 1895-1910.
1112 Jones, S.R., Gainetdinov, R.R., Hu, X.T., Cooper, D.C., Wightman, R.M., White, F.J., and Caron,
1113 M.G. (1999). Loss of autoreceptor functions in mice lacking the dopamine transporter. Nat
1114 Neurosci *2*, 649-655.
1115 Kabsch, W. (2010). Xds. Acta Crystallogr D Biol Crystallogr *66*, 125-132.
1116 Kahlig, K.M., Binda, F., Khoshbouei, H., Blakely, R.D., McMahon, D.G., Javitch, J.A., and Galli,
1117 A. (2005). Amphetamine induces dopamine efflux through a dopamine transporter channel. Proc
1118 Natl Acad Sci U S A *102*, 3495-3500.
1119 Kaiser, M. (2015). Neuroanatomy: connectome connects fly and mammalian brain networks. Curr
1120 Biol *25*, R416-418.
1121 Kazmier, K., Sharma, S., Quick, M., Islam, S.M., Roux, B., Weinstein, H., Javitch, J.A., and
1122 McHaourab, H.S. (2014). Conformational dynamics of ligand-dependent alternating access in
1123 LeuT. Nat Struct Mol Biol *21*, 472-479.
1124 Khelashvili, G., Doktorova, M., Sahai, M.A., Johner, N., Shi, L., and Weinstein, H. (2015a).
1125 Computational modeling of the N-terminus of the human dopamine transporter and its interaction
1126 with PIP2 -containing membranes. Proteins *83*, 952-969.

Khelashvili, G., Stanley, N., Sahai, M.A., Medina, J., LeVine, M.V., Shi, L., De Fabritiis, G., and Weinstein, H. (2015b). Spontaneous inward opening of the dopamine transporter is triggered by PIP2-regulated dynamics of the N-terminus. ACS Chem Neurosci *6*, 1825-1837.

Kirkhart, C., and Scott, K. (2015). Gustatory learning and processing in the Drosophila mushroom bodies. J Neurosci *35*, 5950-5958.

Kniazeff, J., Shi, L., Loland, C.J., Javitch, J.A., Weinstein, H., and Gether, U. (2008). An intracellular interaction network regulates conformational transitions in the dopamine transporter. The Journal of biological chemistry *283*, 17691-17701.

Krishnamurthy, H., and Gouaux, E. (2012). X-ray structures of LeuT in substrate-free outward-open and apo inward-open states. Nature *481*, 469-474.

Kuenze, G., Duran, A.M., Woods, H., Brewer, K.R., McDonald, E.F., Vanoye, C.G., George, A.L., Jr., Sanders, C.R., and Meiler, J. (2019). Upgraded molecular models of the human KCNQ1 potassium channel. PloS one *14*, e0220415.

Kume, K., Kume, S., Park, S.K., Hirsh, J., and Jackson, F.R. (2005). Dopamine is a regulator of arousal in the fruit fly. J Neurosci *25*, 7377-7384.

Kurian, M.A., Li, Y., Zhen, J., Meyer, E., Hai, N., Christen, H.J., Hoffmann, G.F., Jardine, P., von Moers, A., Mordekar, S.R.*, et al.* (2011). Clinical and molecular characterisation of hereditary dopamine transporter deficiency syndrome: an observational cohort and experimental study. Lancet Neurol *10*, 54-62.

Kurian, M.A., Zhen, J., Cheng, S.Y., Li, Y., Mordekar, S.R., Jardine, P., Morgan, N.V., Meyer, E., Tee, L., Pasha, S.*, et al.* (2009). Homozygous loss-of-function mutations in the gene encoding the dopamine transporter are associated with infantile parkinsonism-dystonia. J Clin Invest *119*, 1595-1603.

Lill, C.M. (2016). Genetics of Parkinson's disease. Mol Cell Probes *30*, 386-396.

1151 Loder, M.K., and Melikian, H.E. (2003). The dopamine transporter constitutively internalizes and
1152 recycles in a protein kinase C-regulated manner in stably transfected PC12 cell lines. The Journal
1153 of biological chemistry *278*, 22168-22174.
1154 Mazei-Robison, M.S., Bowton, E., Holy, M., Schmudermaier, M., Freissmuth, M., Sitte, H.H., Galli,
1155 A., and Blakely, R.D. (2008). Anomalous dopamine release associated with a human dopamine
1156 transporter coding variant. J Neurosci *28*, 7040-7046.
1157 McClung, C., and Hirsh, J. (1998). Stereotypic behavioral responses to free-base cocaine and
1158 the development of behavioral sensitization in Drosophila. Curr Biol *8*, 109-112.
1159 McCoy, A.J., Grosse-Kunstleve, R.W., Adams, P.D., Winn, M.D., Storoni, L.C., and Read, R.J.
1160 (2007). Phaser crystallographic software. J Appl Crystallogr *40*, 658-674.
1161 McGregor, M.M., and Nelson, A.B. (2019). Circuit Mechanisms of Parkinson's Disease. Neuron
1162 *101*, 1042-1056.
1163 McHaourab, H.S., Steed, P.R., and Kazmier, K. (2011). Toward the fourth dimension of
1164 membrane protein structure: insight into dynamics from spin-labeling EPR spectroscopy.
1165 Structure *19*, 1549-1561.
1166 Meisenzahl, E.M., Schmitt, G.J., Scheuerecker, J., and Moller, H.J. (2007). The role of dopamine
1167 for the pathophysiology of schizophrenia. Int Rev Psychiatry *19*, 337-345.
1168 Miranda, M., Dionne, K.R., Sorkina, T., and Sorkin, A. (2007). Three ubiquitin conjugation sites in
1169 the amino terminus of the dopamine transporter mediate protein kinase C-dependent endocytosis
1170 of the transporter. Mol Biol Cell *18*, 313-323.
1171 Mou, L., Ding, W., and Fernandez-Funez, P. (2019). Open questions on the nature of Parkinson's
1172 disease: from triggers to spreading pathology. J Med Genet *57*, 73-81.
1173 Murshudov, G.N., Skubak, P., Lebedev, A.A., Pannu, N.S., Steiner, R.A., Nicholls, R.A., Winn,
1174 M.D., Long, F., and Vagin, A.A. (2011). REFMAC5 for the refinement of macromolecular crystal
1175 structures. Acta Crystallogr D Biol Crystallogr *67*, 355-367.
1176 Nagoshi, E. (2018). Drosophila Models of Sporadic Parkinson's Disease. Int J Mol Sci *19*.

1177 Ng, J., Zhen, J., Meyer, E., Erreger, K., Li, Y., Kakar, N., Ahmad, J., Thiele, H., Kubisch, C., Rider,
1178 N.L.*, et al.* (2014). Dopamine transporter deficiency syndrome: phenotypic spectrum from infancy
1179 to adulthood. Brain *137*, 1107-1119.
1180 Palmiter, R.D. (2008). Dopamine signaling in the dorsal striatum is essential for motivated
1181 behaviors: lessons from dopamine-deficient mice. Ann N Y Acad Sci *1129*, 35-46.
1182 Panigrahi, B., Martin, K.A., Li, Y., Graves, A.R., Vollmer, A., Olson, L., Mensh, B.D., Karpova,
1183 A.Y., and Dudman, J.T. (2015). Dopamine Is Required for the Neural Representation and Control
1184 of Movement Vigor. Cell *162*, 1418-1430.
1185 Penmatsa, A., Wang, K.H., and Gouaux, E. (2013). X-ray structure of dopamine transporter
1186 elucidates antidepressant mechanism. Nature *503*, 85-90.
1187 Pettersen, E.F., Goddard, T.D., Huang, C.C., Couch, G.S., Greenblatt, D.M., Meng, E.C., and
1188 Ferrin, T.E. (2004). UCSF Chimera--a visualization system for exploratory research and analysis.
1189 Journal of computational chemistry *25*, 1605-1612.
1190 Phillips, J.C., Braun, R., Wang, W., Gumbart, J., Tajkhorshid, E., Villa, E., Chipot, C., Skeel, R.D.,
1191 Kale, L., and Schulten, K. (2005). Scalable molecular dynamics with NAMD. Journal of
1192 computational chemistry *26*, 1781-1802.
1193 Pitmon, E., Stephens, G., Parkhurst, S.J., Wolf, F.W., Kehne, G., Taylor, M., and Lebestky, T.
1194 (2016). The D1 family dopamine receptor, DopR, potentiates hind leg grooming behavior in
1195 Drosophila. Genes, brain, and behavior *15*, 327-334.
1196 Pizzo, A.B., Karam, C.S., Zhang, Y., Ma, C.L., McCabe, B.D., and Javitch, J.A. (2014).
1197 Amphetamine-induced behavior requires CaMKII-dependent dopamine transporter
1198 phosphorylation. Molecular psychiatry *19*, 279-281.
1199 Politis, M., and Niccolini, F. (2015). Serotonin in Parkinson's disease. Behav Brain Res *277*, 136-
1200 145.
1201 Razavi, A.M., Khelashvili, G., and Weinstein, H. (2018). How structural elements evolving from
1202 bacterial to human SLC6 transporters enabled new functional properties. BMC Biol *16*, 31.

Reith, M.E.A., Jones, K.T., Zhen, J., and Topiol, S. (2018). Latch and trigger role for R445 in DAT transport explains molecular basis of DTDS. Bioorg Med Chem Lett *28*, 470-475.

Riemensperger, T., Isabel, G., Coulom, H., Neuser, K., Seugnet, L., Kume, K., Iche-Torres, M., Cassar, M., Strauss, R., Preat, T.*, et al.* (2011). Behavioral consequences of dopamine deficiency in the Drosophila central nervous system. Proc Natl Acad Sci U S A *108*, 834-839.

Robertson, S.D., Matthies, H.J., and Galli, A. (2009). A closer look at amphetamine-induced reverse transport and trafficking of the dopamine and norepinephrine transporters. Mol Neurobiol *39*, 73-80.

Russo, S.J., and Nestler, E.J. (2013). The brain reward circuitry in mood disorders. Nat Rev Neurosci *14*, 609-625.

Sadaf, S., Reddy, O.V., Sane, S.P., and Hasan, G. (2015). Neural control of wing coordination in flies. Curr Biol *25*, 80-86.

Salvatore, M.F., Calipari, E.S., and Jones, S.R. (2016). Regulation of Tyrosine Hydroxylase Expression and Phosphorylation in Dopamine Transporter-Deficient Mice. ACS Chem Neurosci *7*, 941-951.

Shan, J., Javitch, J.A., Shi, L., and Weinstein, H. (2011). The substrate-driven transition to an inward-facing conformation in the functional mechanism of the dopamine transporter. PloS one *6*, e16350.

Shekar, A., Aguilar, J.I., Galli, G., Cozzi, N.V., Brandt, S.D., Ruoho, A.E., Baumann, M.H., Matthies, H.J., and Galli, A. (2017). Atypical dopamine efflux caused by 3,4-methylenedioxypyrovalerone (MDPV) via the human dopamine transporter. J Chem Neuroanat *83-84*, 69-74.

Stolzenberg, S., Quick, M., Zhao, C., Gotfryd, K., Khelashvili, G., Gether, U., Loland, C.J., Javitch, J.A., Noskov, S., Weinstein, H.*, et al.* (2015). Mechanism of the Association between Na+ Binding and Conformations at the Intracellular Gate in Neurotransmitter:Sodium Symporters. The Journal of biological chemistry *290*, 13992-14003.

1229 Swanson, J.M., Kinsbourne, M., Nigg, J., Lanphear, B., Stefanatos, G.A., Volkow, N., Taylor, E.,
1230 Casey, B.J., Castellanos, F.X., and Wadhwa, P.D. (2007). Etiologic subtypes of attention-
1231 deficit/hyperactivity disorder: brain imaging, molecular genetic and environmental factors and the
1232 dopamine hypothesis. Neuropsychol Rev *17*, 39-59.
1233 Taylor, T.N., Greene, J.G., and Miller, G.W. (2010). Behavioral phenotyping of mouse models of
1234 Parkinson's disease. Behav Brain Res *211*, 1-10.
1235 Trinh, J., and Farrer, M. (2013). Advances in the genetics of Parkinson disease. Nat Rev Neurol
1236 *9*, 445-454.
1237 Trinh, K., Moore, K., Wes, P.D., Muchowski, P.J., Dey, J., Andrews, L., and Pallanck, L.J. (2008).
1238 Induction of the phase II detoxification pathway suppresses neuron loss in Drosophila models of
1239 Parkinson's disease. J Neurosci *28*, 465-472.
1240 Turner, R.S., and Desmurget, M. (2010). Basal ganglia contributions to motor control: a vigorous
1241 tutor. Curr Opin Neurobiol *20*, 704-716.
1242 van den Berg, C., Beek, P.J., Wagenaar, R.C., and van Wieringen, P.C. (2000). Coordination
1243 disorders in patients with Parkinson's disease: a study of paced rhythmic forearm movements.
1244 Exp Brain Res *134*, 174-186.
1245 Wang, J.W., Beck, E.S., and McCabe, B.D. (2012). A modular toolset for recombination
1246 transgenesis and neurogenetic analysis of Drosophila. PloS one *7*, e42102.
1247 Wang, K.H., Penmatsa, A., and Gouaux, E. (2015). Neurotransmitter and psychostimulant
1248 recognition by the dopamine transporter. Nature *521*, 322-327.
1249 Weintraub, D., Koester, J., Potenza, M.N., Siderowf, A.D., Stacy, M., Voon, V., Whetteckey, J.,
1250 Wunderlich, G.R., and Lang, A.E. (2010). Impulse control disorders in Parkinson disease: a cross-
1251 sectional study of 3090 patients. Arch Neurol *67*, 589-595.
1252 Weyerhauser, P., Kantelhardt, S.R., and Kim, E.L. (2018). Re-purposing Chloroquine for
1253 Glioblastoma: Potential Merits and Confounding Variables. Front Oncol *8*, 335.

1254 Whitworth, A.J., Theodore, D.A., Greene, J.C., Benes, H., Wes, P.D., and Pallanck, L.J. (2005).
1255 Increased glutathione S-transferase activity rescues dopaminergic neuron loss in a Drosophila
1256 model of Parkinson's disease. Proc Natl Acad Sci U S A *102*, 8024-8029.
1257 Winn, M.D., Isupov, M.N., and Murshudov, G.N. (2001). Use of TLS parameters to model
1258 anisotropic displacements in macromolecular refinement. Acta Crystallogr D Biol Crystallogr *57*,
1259 122-133.
1260 Wu, E.L., Cheng, X., Jo, S., Rui, H., Song, K.C., Dávila-Contreras, E.M., Qi, Y., Lee, J., Monje-
1261 Galvan, V., and Venable, R.M. (2014). CHARMM-GUI membrane builder toward realistic
1262 biological membrane simulations. Journal of computational chemistry *35*, 1997-2004.
1263 Wu, S., Bellve, K.D., Fogarty, K.E., and Melikian, H.E. (2015). Ack1 is a dopamine transporter
1264 endocytic brake that rescues a trafficking-dysregulated ADHD coding variant. Proc Natl Acad Sci
1265 U S A *112*, 15480-15485.
1266 Xiong, Y., and Yu, J. (2018). Modeling Parkinson's Disease in Drosophila: What Have We
1267 Learned for Dominant Traits? Front Neurol *9*, 228.
1268 Yamamoto, S., and Seto, E.S. (2014). Dopamine dynamics and signaling in Drosophila: an
1269 overview of genes, drugs and behavioral paradigms. Experimental animals *63*, 107-119.
1270 Yamashita, A., Singh, S.K., Kawate, T., Jin, Y., and Gouaux, E. (2005). Crystal structure of a
1271 bacterial homologue of Na+/Cl--dependent neurotransmitter transporters. Nature *437*, 215-223.
1272 Zabalax, F.A., Card, G.M., Fontaine, E.I., Murray, R.M., and Dickinson, M.H. (2008). Dynamics
1273 of escaping flight initiations of Drosophila melanogaster. Paper presented at: 2008 2nd IEEE RAS
1274 & EMBS International Conference on Biomedical Robotics and Biomechatronics.
1275 Zou, P., and McHaourab, H.S. (2010). Increased sensitivity and extended range of distance
1276 measurements in spin-labeled membrane proteins: Q-band double electron-electron resonance
1277 and nanoscale bilayers. Biophysical journal *98*, L18-20.

1278

Figure 1

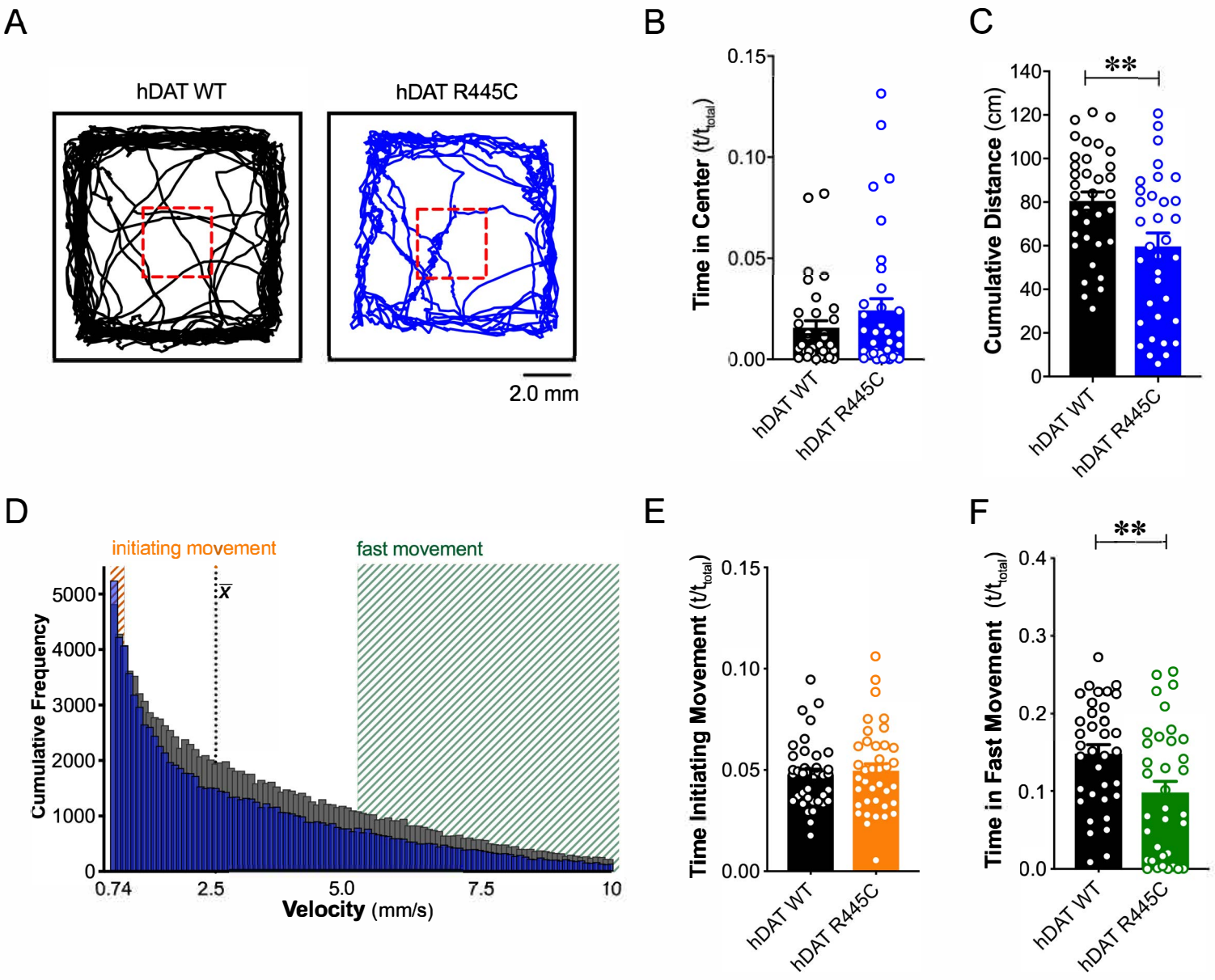

Figure 2

A

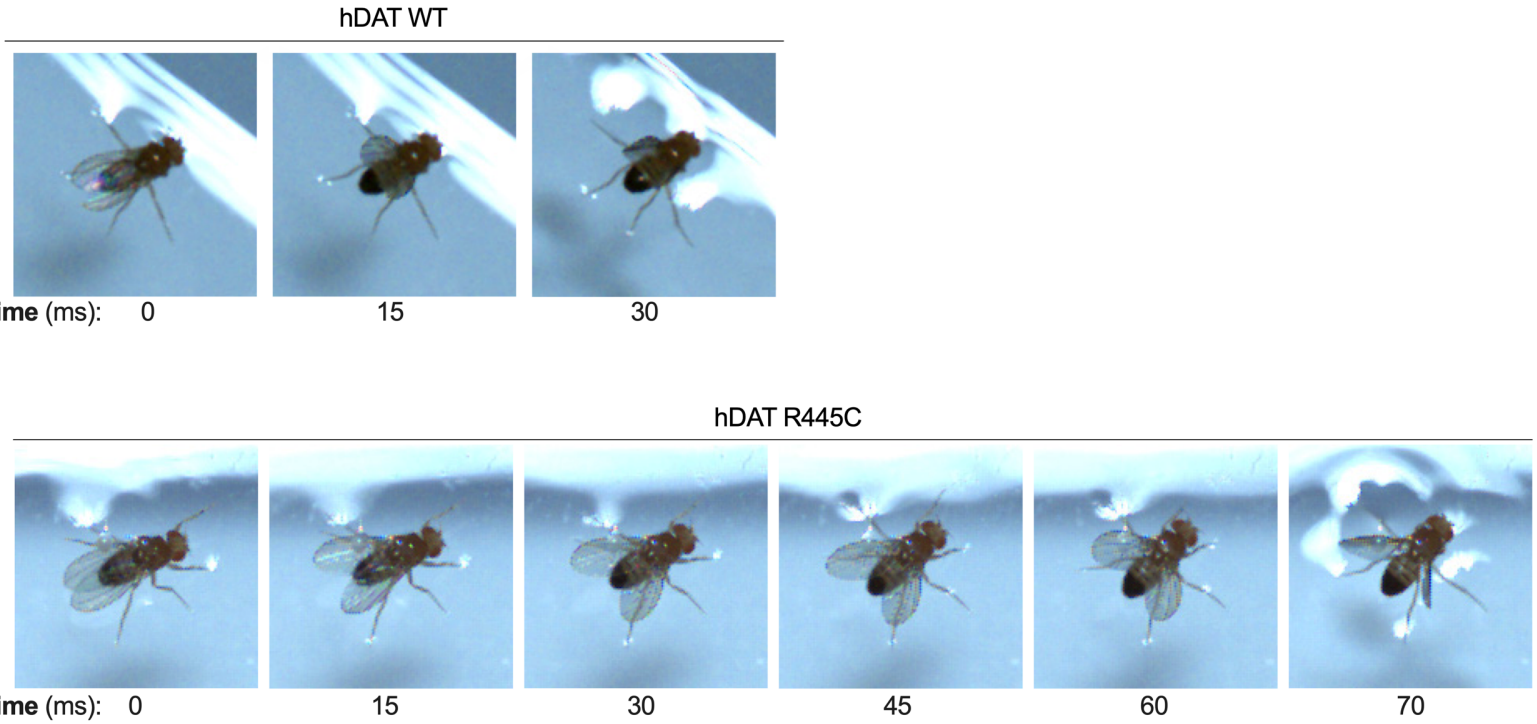

B

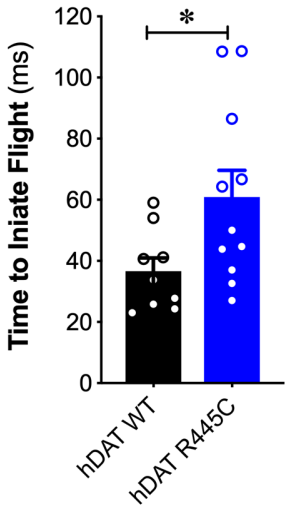

C

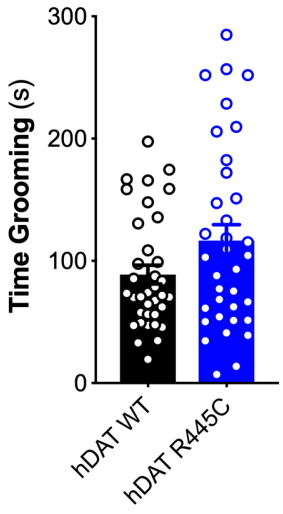

Figure 3

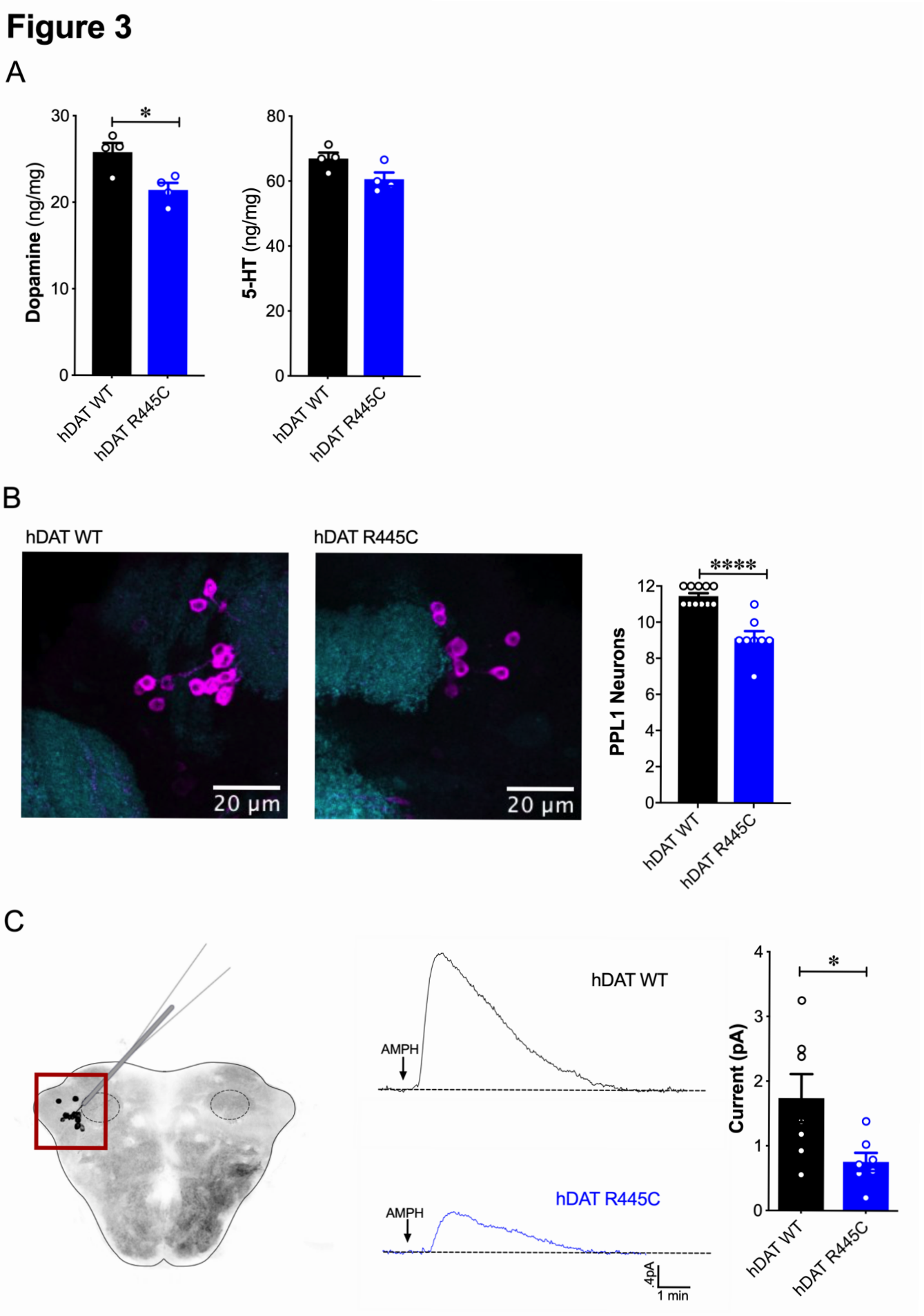

Figure 4

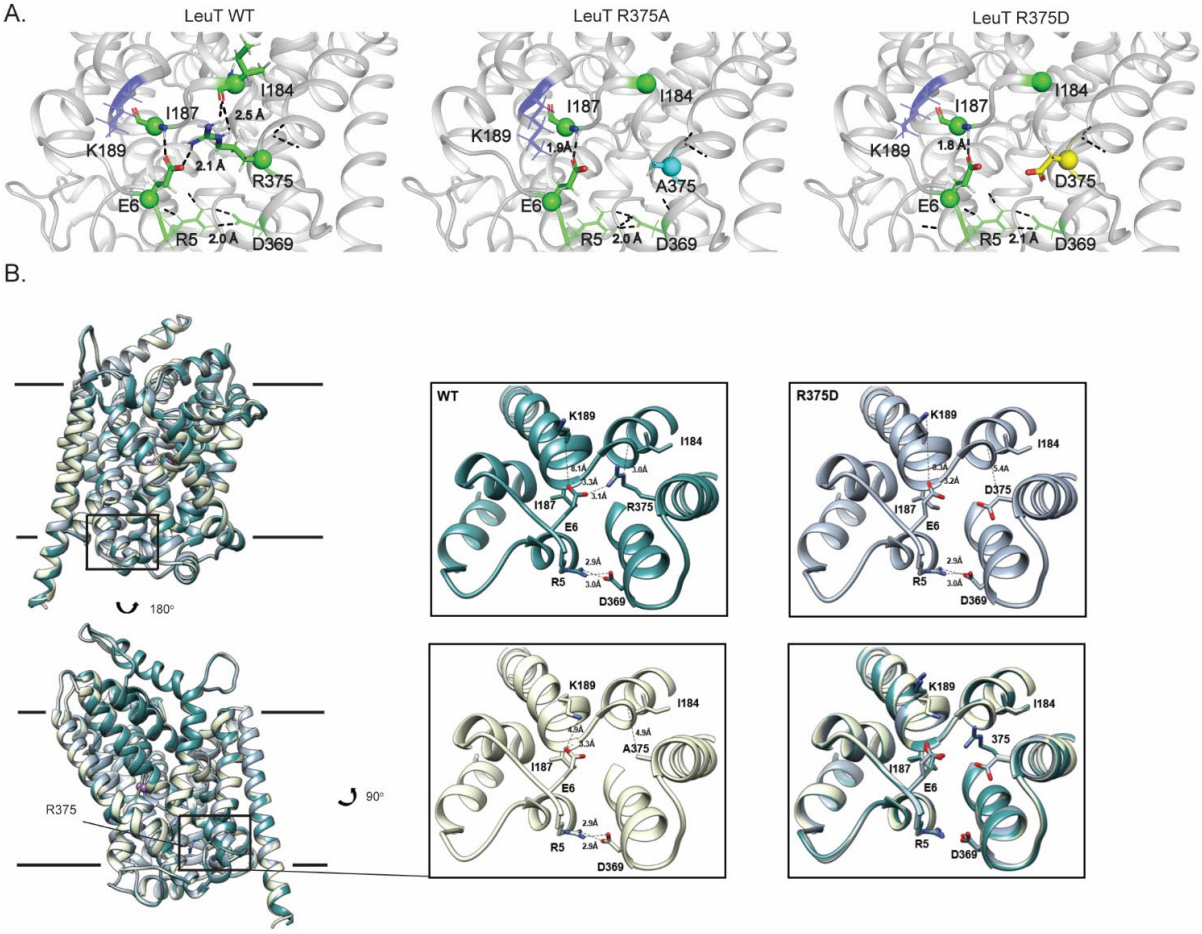

Figure 5

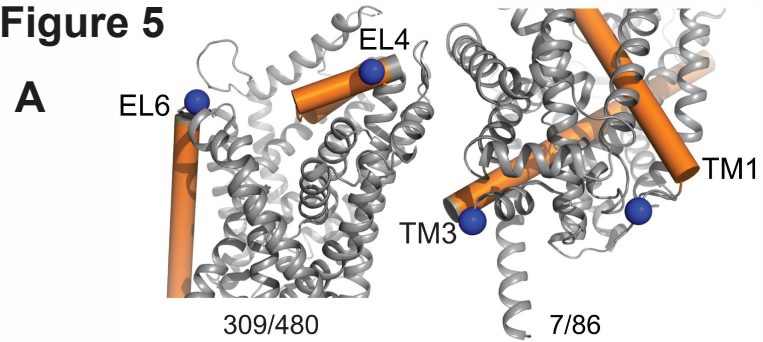
A
EL4
EL6
TM1
TM3
309/480
7/86

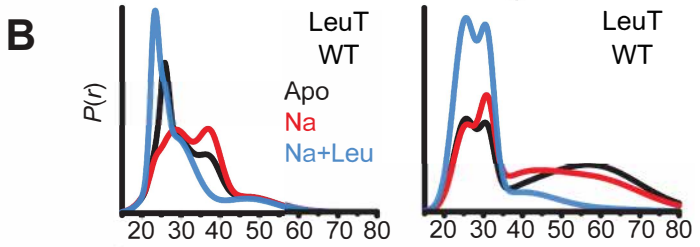
B
LeuT
WT
Apo
Na
Na+Leu
P(r)
20 30 40 50 60 70 80
LeuT
WT
20 30 40 50 60 70 80

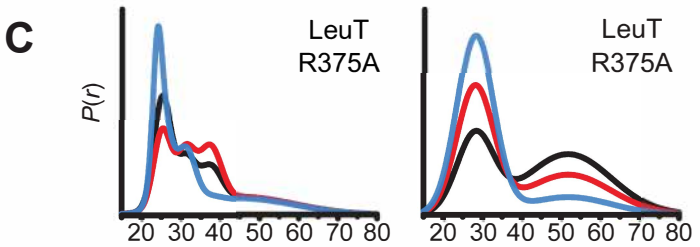
C
LeuT
R375A
P(r)
20 30 40 50 60 70 80
LeuT
R375A
20 30 40 50 60 70 80

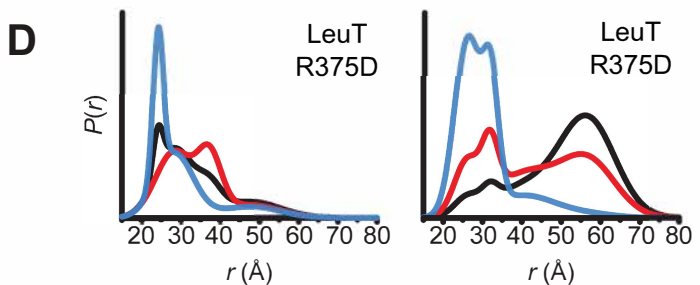
D
LeuT
R375D
P(r)
20 30 40 50 60 70 80
r (Å)
LeuT
R375D
20 30 40 50 60 70 80
r (Å)

Figure 6

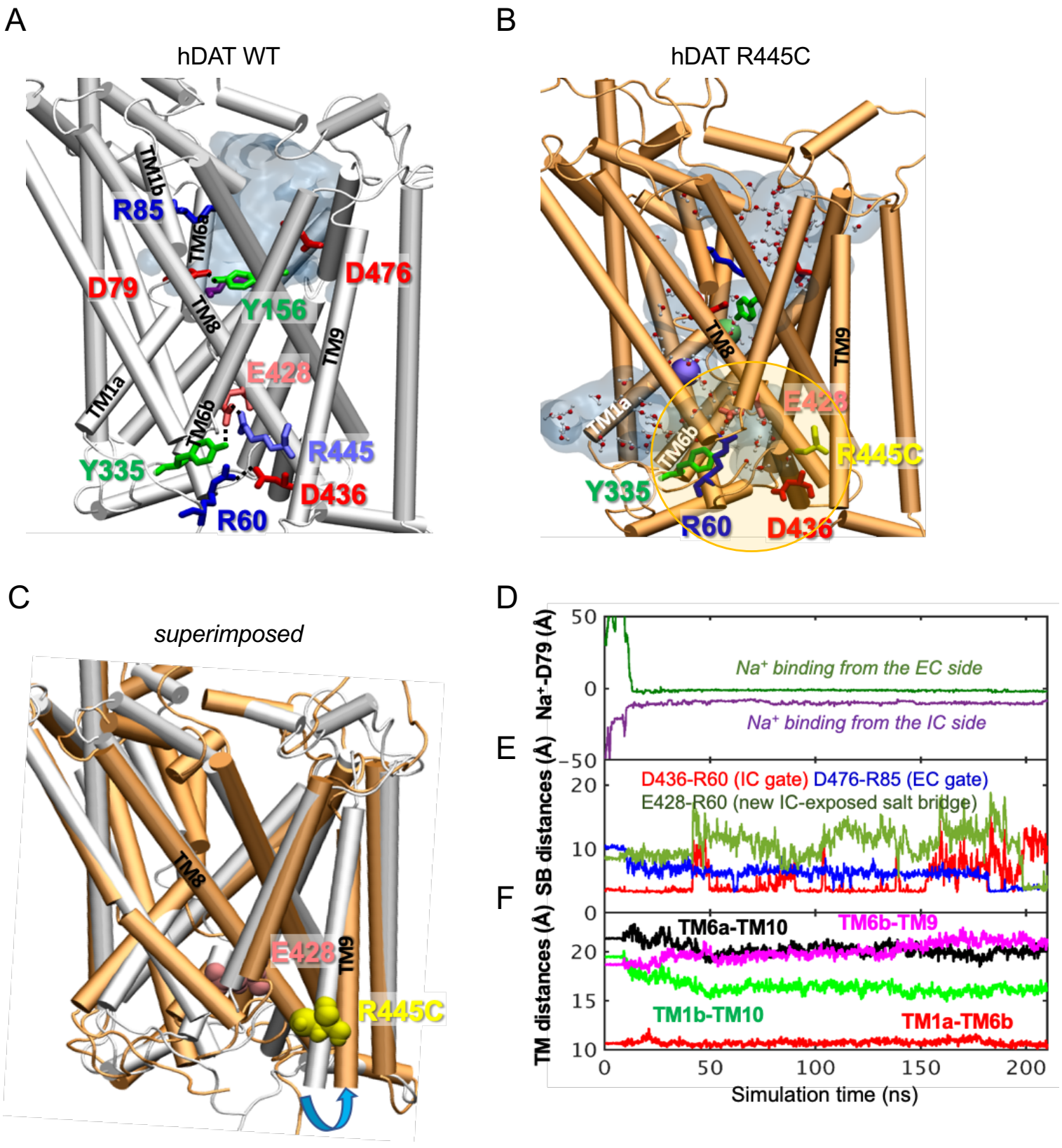

Figure 7

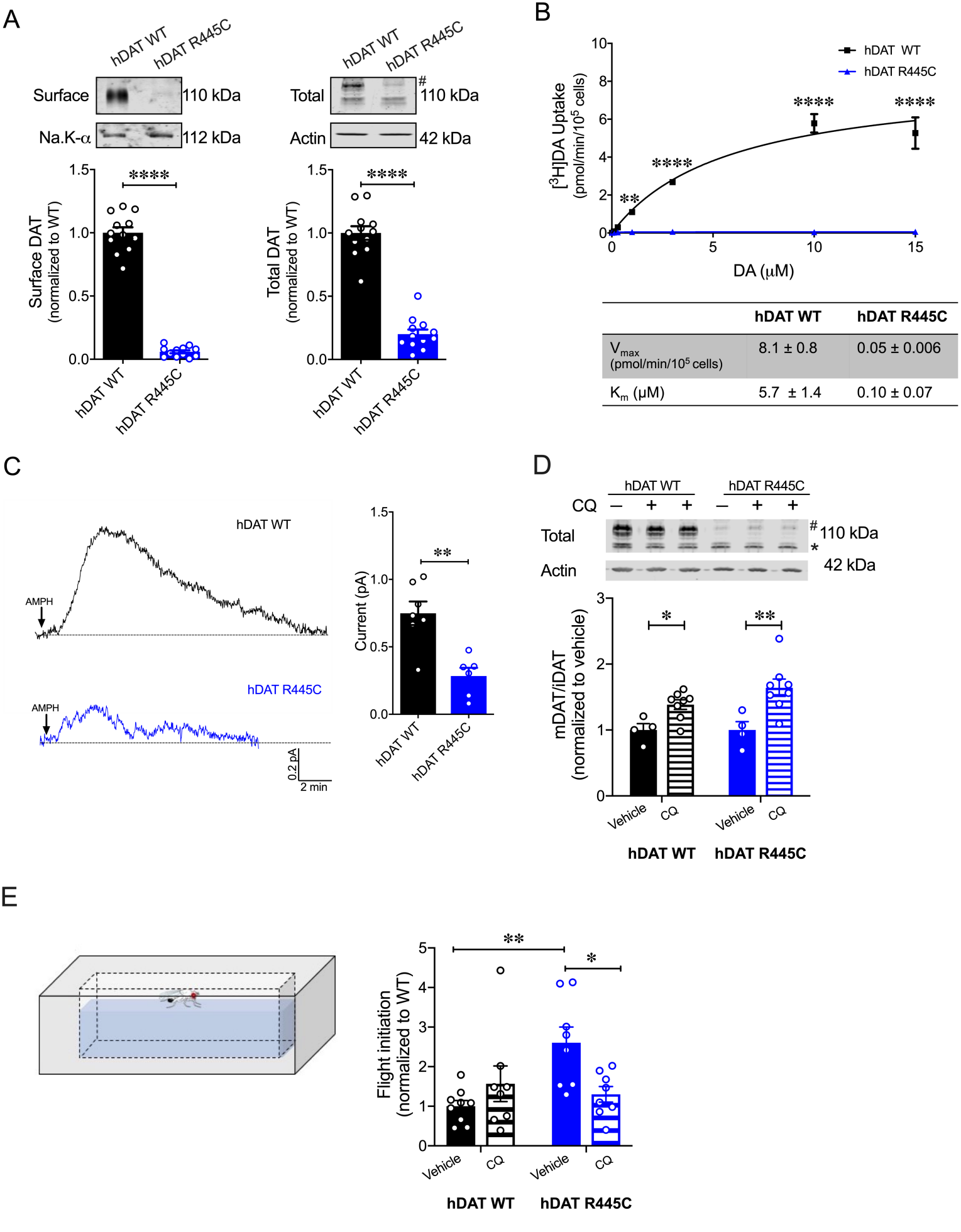

	hDAT WT	hDAT R445C
V_{max} (pmol/min/10^5 cells)	8.1 ± 0.8	0.05 ± 0.006
K_m (μM)	5.7 ± 1.4	0.10 ± 0.07

Supplementary Figure 1: AMPH-induced DA efflux and behaviors in hDAT WT flies.

(**A**) (*top*) AMPH-induced (arrow) amperometric currents in DAT^{fmn}, dDAT, and hDAT WT brains. In hDAT WT brains, cocaine (20 μM) blocked the ability of AMPH to cause DA efflux. (*bottom*) Quantitation of peak currents showed a significant decrease in DA efflux measured in DAT^{fmn} relative to dDAT and hDAT WT brains, as well as in hDAT WT brains in the presence of cocaine. ($F_{(3,18)}$ = 9.341, p = 0.0006; n = 3-7). (**B**) DA uptake in intact brains of DAT^{fmn}, dDAT, and hDAT WT flies ($F_{(2,9)}$ = 25.75, p = 0.0002; n = 4). (**C**) AMPH-induced locomotion measured by beam crossing detection recorded over a 60 min time period in DAT^{fmn}, dDAT and hDAT WT flies (Interaction $F_{(2,24)}$ =52.66, p<0.0001; n = 5. Data represent mean ± SEM. One-way ANOVA with Tukey's multiple comparison test (A)-(B); Two-way ANOVA with Tukey's multiple comparison test (C). * p<0.05; ** p<0.01; *** p<0.001; **** p<0.0001.

Supplementary Figure 2: Related to Fig 4A.

(**A**) Distances between IC residues in angstroms (Å) for LeuT WT, R375A, R375C, and R375D. (**B**) Rosetta scores represent the average scores of the top 5% of models. ΔΔG values are in Rosetta Energy Units (REUs). (**C**) Rosetta modeling of LeuT R375C, where protein backbones are represented in *grey*, amino acid side chains in *green*, K189 in *blue* and R375C in *magenta*. All corresponding polar contacts between side chain or backbone atoms in each model are represented as dashed lines in *black*. (**D**) REU versus RMSD diagrams were obtained from 1000 Rosetta Flex ΔΔG trajectories for LeuT WT (*left*) and LeuT R375A (*right*)**.** The RMSD between the protein backbone and heavy side chain atoms within a 10 Å distance of R375 and R375A was calculated to show the correlation between the energy-optimized models and the experimental model.

Supplementary Figure 3: Related to Fig 4B.

Crystallographic data for LeuT WT and R375A regarding data collection, model building, and refinement statistics.

Supplementary Figure 4: Related to Fig 6.

(**A**) Model of hDAT R445D showing the formation of a channel-like intermediate promoted by the opening of the IC vestibule. In hDAT R445D, three Na^+ ions bind along the transport lumen (two diffusing from the IC region, and one from the EC region). The region enclosed in the yellow ellipse is more exposed to the cytosol relative to WT, allowing Na^+ and water entry. Hydrated regions inside the transporter are indicated in *gray* shaded areas with explicit water molecules displayed in spheres and lines (CPK format). The conformation shown is a snapshot (100 ns) taken from the simulation trajectory illustrated in B-D**.** (**B**) Time evolution of distances between Na^+ and D79. (**C**) Time evolution of distances between the D476-R85 salt-bridge on the EC side show that this interaction shortens over time (EC gate closure). The distances between D436-R60 on the IC side increase intermittently (IC gate opening). Interestingly, a new salt bridge between D445 and K257 is formed intermittently. (**D**) Time evolution of interhelical distances between EC-exposed TM1b-TM10 and TM6a-TM10 shows that the EC region remains exposed to solvent with reduced opening, whereas IC-exposed TM1a-TM6b shows that the IC region is predominantly closed with a slight opening indicated by the increase in TM6b-TM9 distance.

Supplementary Figure 5: R445A substitution impairs hDAT expression and function.

(**A**) Representative immunoblots of surface hDAT (*top left*), total hDAT (*top right*) and corresponding Na-K ATPase (*bottom left)* and actin (*bottom right)* loading controls (n = 4, in triplicate). hDAT expression was normalized to hDAT WT. hDAT R445A displayed significantly impaired surface ($p < 0.0001$) and total (#) expression relative to hDAT WT ($p < 0.0001$).

(**B**) [^{3}H]DA saturation curves of DA uptake measured in hDAT WT (*black*) and hDAT R445A (*red*) cells (n = 3, in triplicate). Curves were fit to Michaelis-Menten kinetics to derive K_m and V_{max}. DA

uptake for hDAT R445A was significantly reduced compared with hDAT WT ($F_{(5,92)}$ = 22.7, p < 0.0001) as were kinetic constants, K_m and V_{max} (p < 0.0001). (**C**) Left: Representative amperometric traces (DA efflux) recorded in response to AMPH application (10 μM, indicated by arrow) from hDAT WT (*black*) and hDAT R445A (*red*) loaded with DA (2 mM, 10 min) via a whole-cell patch electrode in current-clamp. Right: Quantitation of peak amperometric current in hDAT R445A and hDAT WT cells (p = 0.002; n = 6). Data represent mean ± SEM. Welch's t-test (A); Two-way ANOVA with Bonferroni's multiple comparison test: (B). Mann-Whitney Test (C).

Supplementary Figure 6: R445D substitution impairs hDAT expression and function.

(**A**) Representative immunoblots of surface hDAT (top *left*), total hDAT (top *right*) and corresponding Na-K ATPase (*bottom left)* and actin (*bottom right)* loading controls (n = 4, in triplicate). hDAT R445D displayed significantly reduced surface (p < 0.0001) and total (#) expression relative hDAT WT (p < 0.0001). (**B**) [^{3}H]DA uptake was measured in hDAT WT (*black*), hDAT R445D (*green*) cells (n = 3, in triplicate). Curves were fit to Michaelis-Menten kinetics to derive K_m and V_{max}. DA uptake for hDAT R445D was significantly reduced compared with hDAT WT ($F_{(5,94)}$ = 42.1, p < 0.0001), as were the kinetic constants, K_m and V_{max} (p < 0.0001). (**C**) Left: Representative amperometric traces (DA efflux) recorded in response to AMPH application (10 μM, indicated by arrow) from hDAT WT (*black*) and hDAT R445D (*green*) cells loaded DA (2 mM, 10 min) with a whole-cell patch electrode. Right: Peak current amplitudes illustrated a significant reduction in DA efflux recorded from hDAT R445D relative hDAT WT (p = 0.002; n = 6).

Data represent mean ± SEM. Welch's t-test (A); Two-way ANOVA with Bonferroni's multiple comparison test: (B). Mann-Whitney Test (C).

Supplementary Movies: hDAT WT and hDAT R445C flies in flight.

Media illustrates hDAT WT and hDAT R445C flies initiating flight. Media was recorded using a high-speed camera (2000 fps). Videos displayed are slowed down from the “start” to “stop” time of take-off to ease visualization.

Supplementary Figure 1

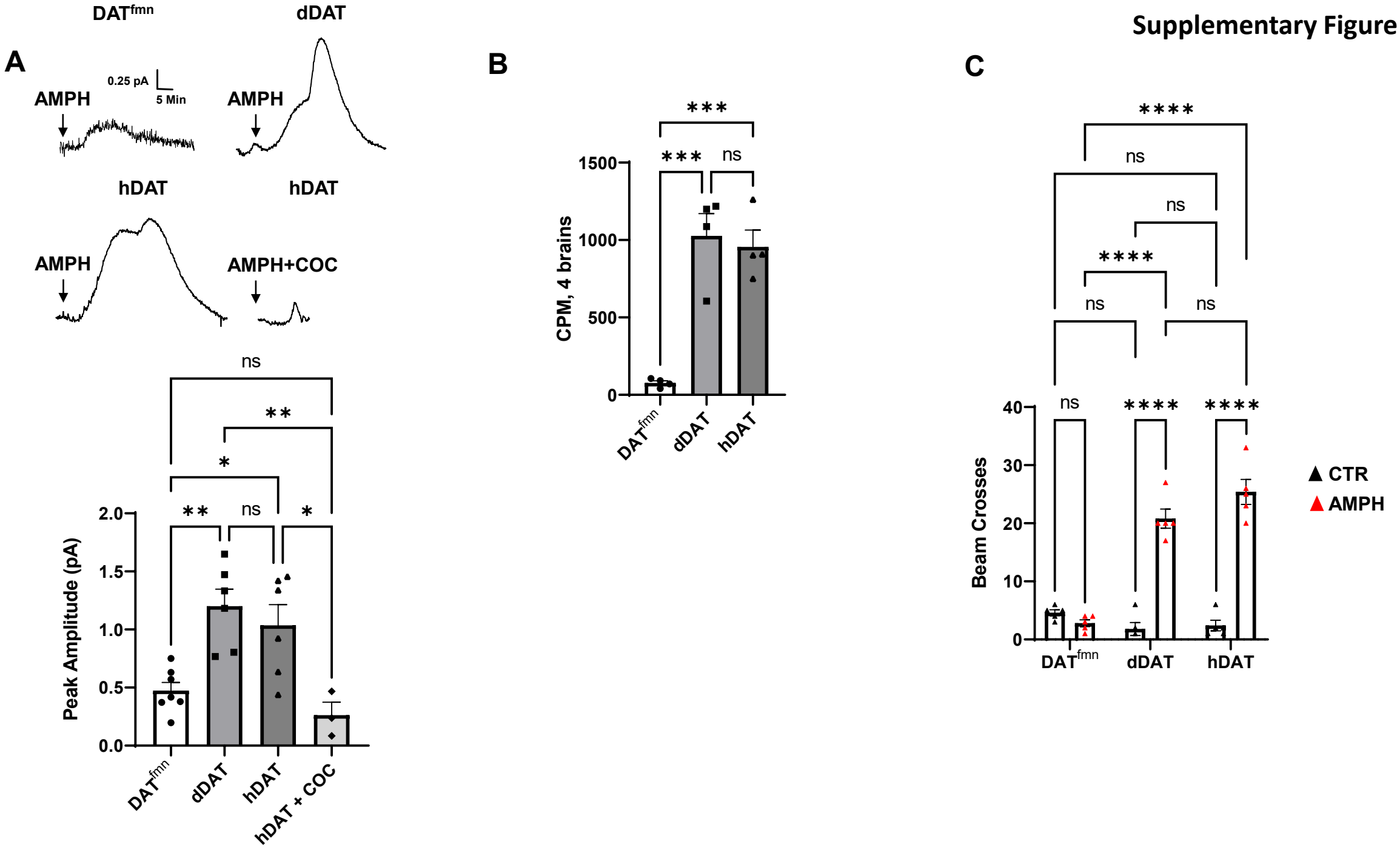

Supplementary Figure 2

A

Rosetta Distance Calculations of LeuT R375A/C/D

	WT	R375A	R375C	R375D
	distance (Å)			
R375-I184	2.5	6	3.3	4.7
R375-E6	2.1	5.4	5.7	4.2
E6-I187	1.9	1.9	1.9	1.8
R5-D369	2	2	2.1	2.1
K189-E6	8.2	7.0	9.9	8.5

B

Rosetta ΔΔG Calculations of LeuT R375A/C/D

WT	R375A		R375C		R375D	
score	score	ΔΔG	score	ΔΔG	score	ΔΔG
-2300.2 ± 4.4	-2295.8 ± 4.3	4.4	-2295.4 ± 4.5	4.8	-2294.6 ± 5.2	5.6

C

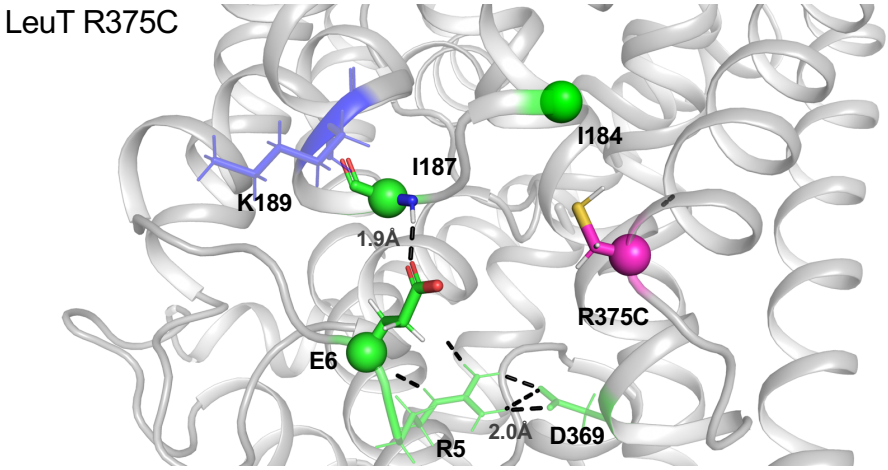

D

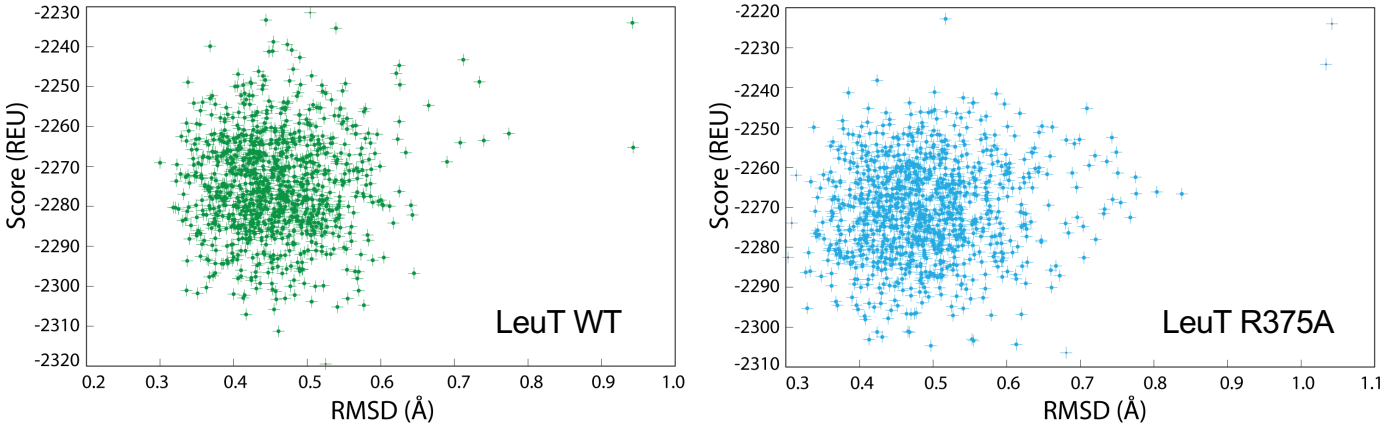

Supplementary Figure 3

	LeuT WT	LeuT R375A	LeuT R375D
PDB ID:	7LQJ	7LQK	7LQL
Data collection			
Space group	C121	C121	C121
Cell dimensions			
a, *b*, *c* (Å)	88.48, 86.87, 81.14	87.58, 86.62, 80.99	86.63, 87.06, 80.59
α, β, γ (°)	90.00, 96.09, 90.00	90.00, 95.64, 90.00	90.00, 95.32, 90.00
Resolution (Å)	43.99 – 2.1	47.31 – 2.1	47.22 – 2.6
R_{sym} or R_{merge}	0.06 (0.54)	0.06 (0.86)	0.26 (2.18)
I / σI	14.9 (3.0)	11.8 (1.6)	7.6(2)
CC1/2	0.99 (0.89)	0.99 (0.71)	0.99 (0.69)
Completeness (%)	99.4 (93.5)	100 (100)	99 (98.9)
Redundancy	7.1 (6.9)	5.1 (5.2)	7.1 (7.4)
Refinement			
Resolution (Å)	43.43 – 2.14	43.58– 2.1	43.53– 2.6
No. reflections	33365	35211	18223
R_{work} / R_{free}	17.77/20.34	18.79/20.92	19.89/23.99
No. atoms	4247	4170	4085
Protein	4019	4011	3976
Ligand/ion			
Ligand	94	102	77
Na	2	2	2
water	135	57	32
B-factors	47.75	52.63	55.03
Protein	46.54	51.55	54.67
Ligand/ion	84.95	94.62	74.36
R.m.s. deviations			
Bond lengths (Å)	0.009	0.004	0.006
Bond angles (°)	0.92	0.63	0.69
Ramachandran (%)			
Favored	97.60	98.20	95.77
Allowed	2.40	1.80	4.02
Disallowed	0.00	0.00	0.20

Supplementary Figure 4

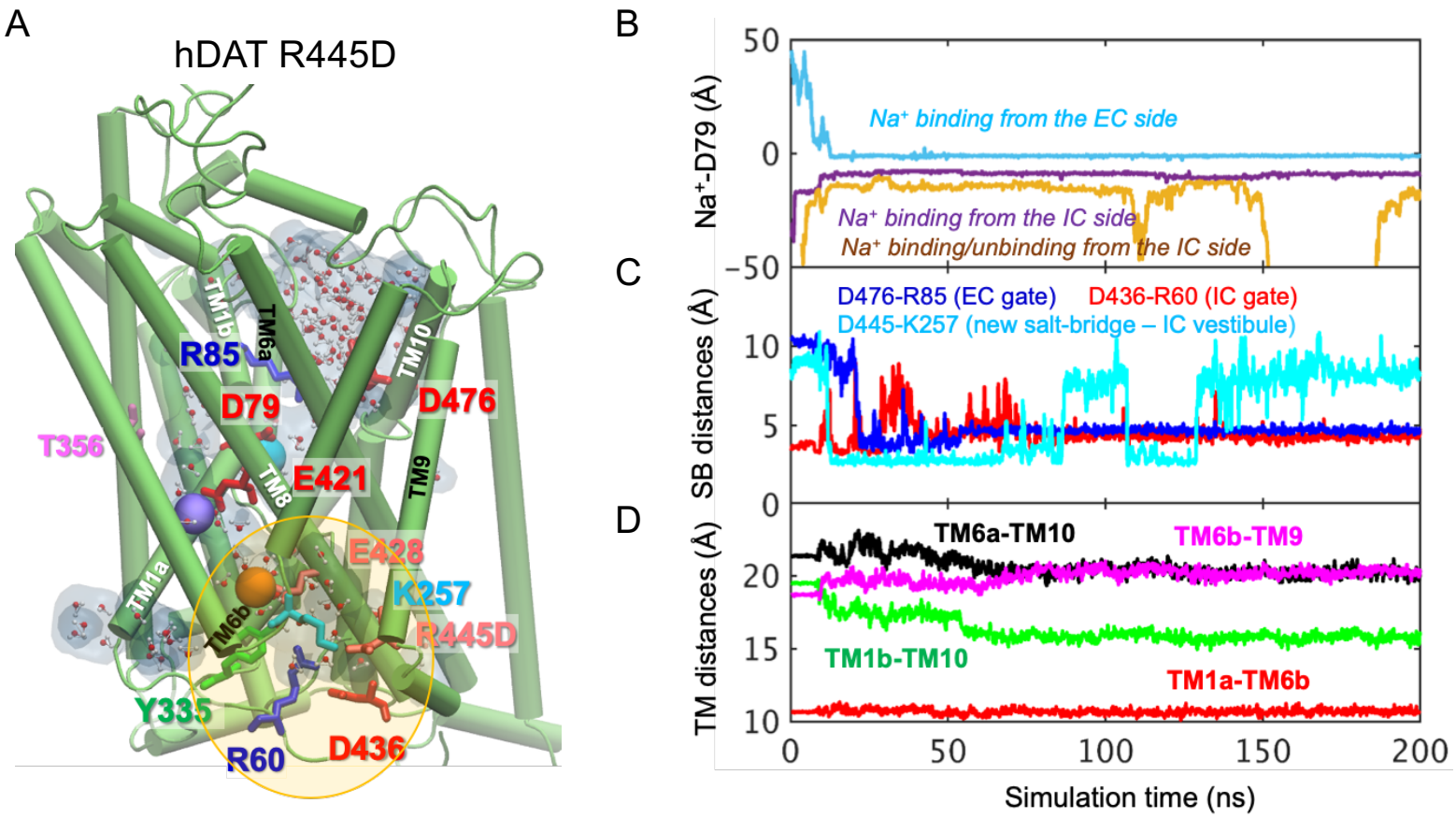

Supplementary Figure 5

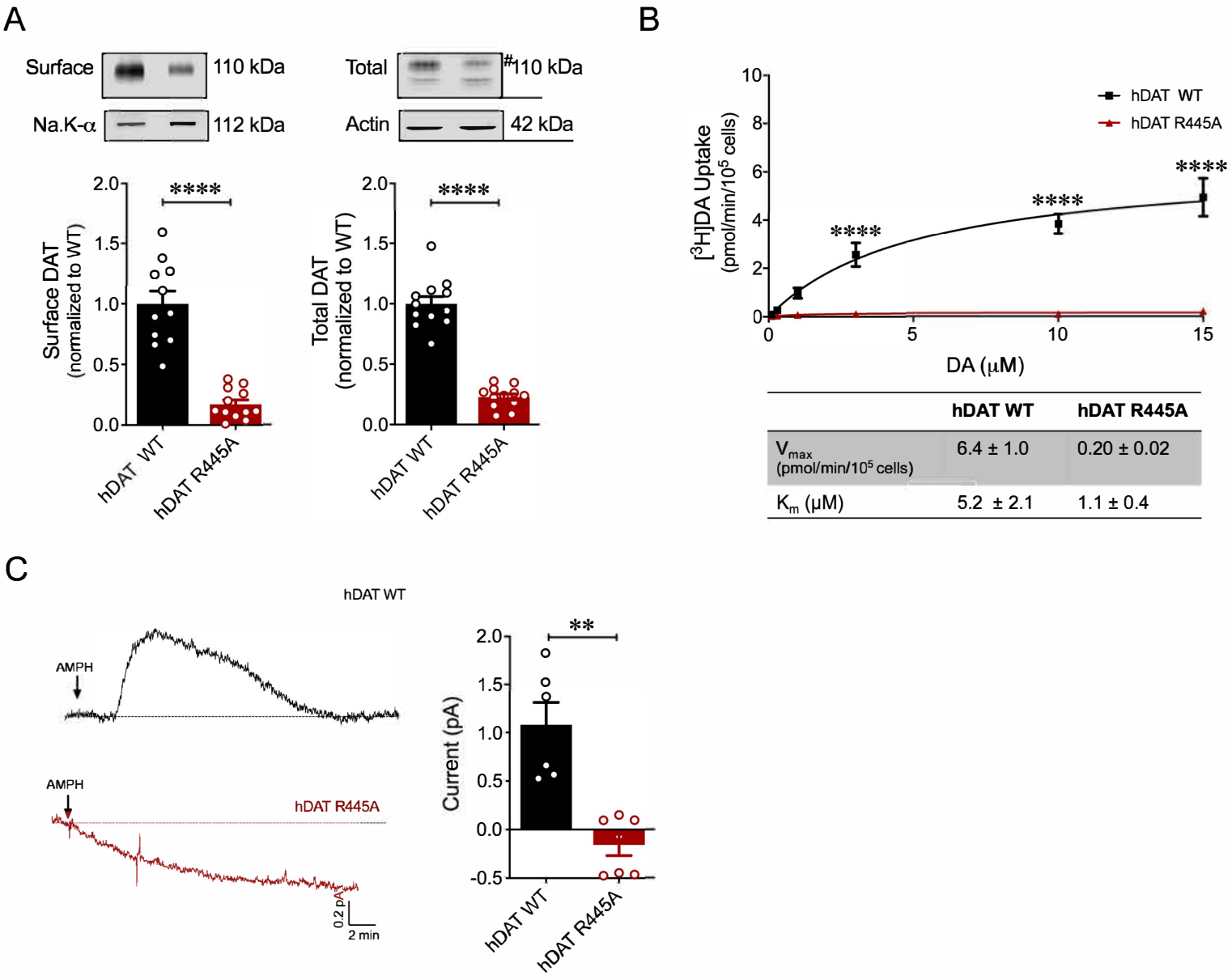

	hDAT WT	hDAT R445A
V_{max} (pmol/min/10^5 cells)	6.4 ± 1.0	0.20 ± 0.02
K_m (μM)	5.2 ± 2.1	1.1 ± 0.4

Supplementary Figure 6

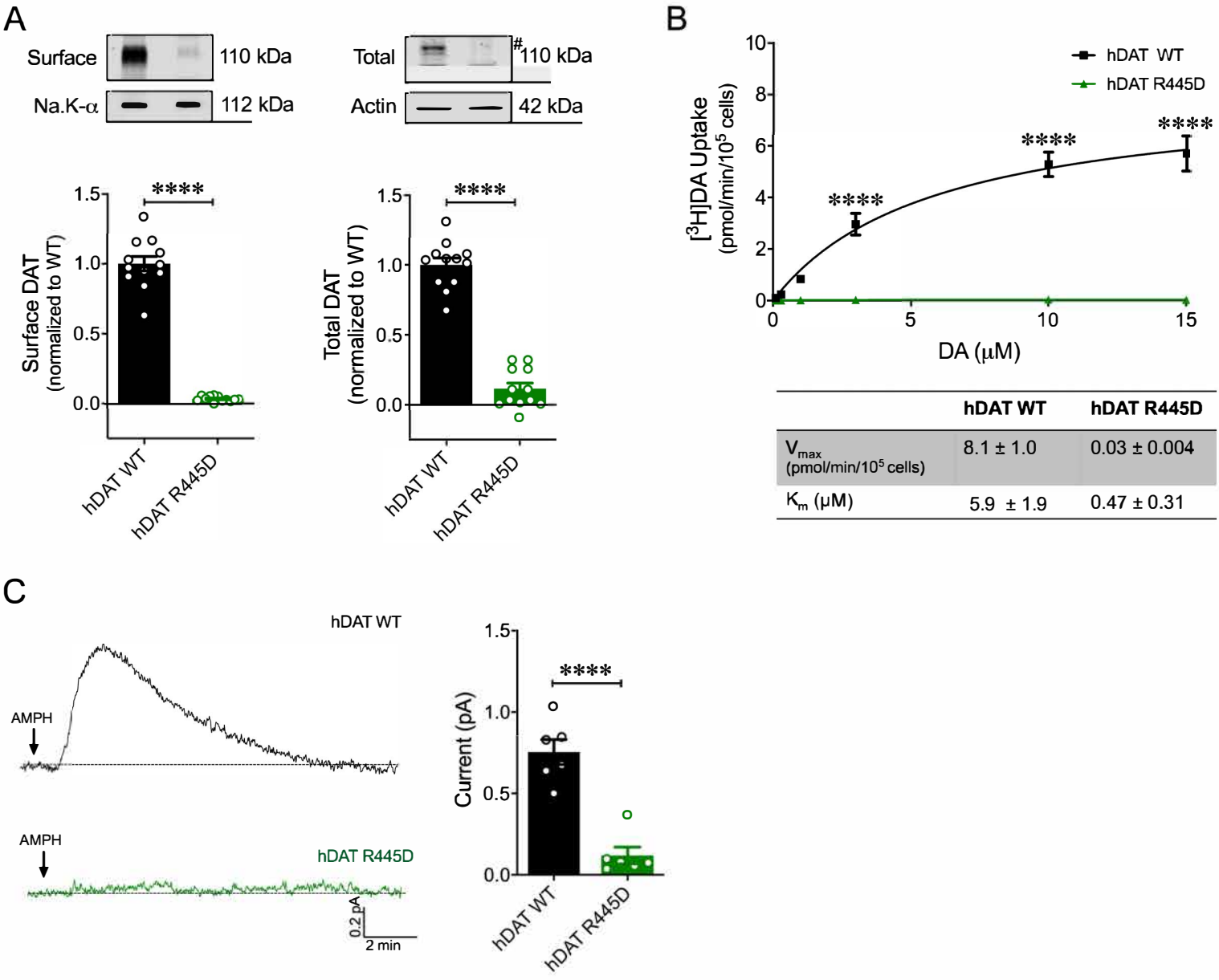

	hDAT WT	hDAT R445D
V_{max} (pmol/min/10^5 cells)	8.1 ± 1.0	0.03 ± 0.004
K_m (μM)	5.9 ± 1.9	0.47 ± 0.31